HHS Public Access

Author manuscript

IEEE Trans Biomed Circuits Syst. Author manuscript; available in PMC 2023 May 09.

Published in final edited form as:

IEEE Trans Biomed Circuits Syst. 2022 February ; 16(1): 64–78. doi:10.1109/TBCAS.2022.3140591.

Design and Optimization of Ultrasonic Links with Phased Arrays for Wireless Power Transmission to Biomedical Implants

Zeinab Kashani [Student Member, IEEE],
School of Electrical Engineering and Computer Science at the Pennsylvania State University, University Park, PA 16802, USA

Sheikh Jawad Ilham [Student Member, IEEE],
School of Electrical Engineering and Computer Science at the Pennsylvania State University, University Park, PA 16802, USA

Mehdi Kiani [Senior Member, IEEE]
School of Electrical Engineering and Computer Science at the Pennsylvania State University, University Park, PA 16802, USA

Abstract

Ultrasound (US) is an attractive modality for wireless power transfer (WPT) to biomedical implants with millimeter (mm) dimensions. To compensate for misalignments in WPT to a mm-sized implant (or powering a network of mm-sized implants), a US transducer array should electronically be driven in a beamforming fashion (known as US phased array) to steer focused US beams at different locations. This paper presents the theory and design methodology of US WPT links with phased arrays and mm-sized receivers (Rx). For given constraints imposed by the application and fabrication, such as load (R_L) and focal distance (F), the optimal geometries of a US phased array and Rx transducer, as well as the optimal operation frequency (f_c) are found through an iterative design procedure to maximize the power transfer efficiency (PTE). An optimal figure of merit (FoM) related to PTE is proposed to simplify the US array design. A design example of a US link is presented and optimized for WPT to a mm-sized Rx with a linear array. In measurements, the fabricated 16-element array (10.9×9×1.7 mm^3) driven by 100 V pulses at f_c of 1.1 MHz with optimal delays for focusing at F = 20 mm generated a US beam with a pressure output of 0.8 MPa. The link could deliver up to 6 mW to a ~ 1 mm^3 Rx with a PTE of 0.14% (R_L = 850 Ω). The beam steering capability of the array at −45° to 45° angles was also characterized.

Index Terms—

Ultrasonic wireless power transfer; linear array; miniaturized implants; misalignment; beam focusing

*Corresponding author: M. Kiani, phone: 814-867-5753, mkiani@psu.edu.

I. Introduction

Wireless power transfer (WPT) to biomedical implants can eliminate their need for bulky batteries or drastically reduce the size of their rechargeable batteries [1]. This can lead to further implant miniaturization to millimeter (mm) scales, thereby reducing the tissue damage and increasing the implant's overall lifetime [2]. A power-efficient, robust, and safe WPT method for powering deeply implanted mm-sized devices can open up new diagnostic and therapeutic applications in the biomedical field, particularly in the promising field of bioelectronic medicine [3]. Currently, WPT can be realized with different modalities, such as magnetic/electric fields and ultrasound (US).

Inductive coupling using low-frequency magnetic fields (several MHz and below), which is the conventional method for WPT, is highly efficient when the implant size is in the centimeter (cm) range or comparable to the powering distance [4]-[6]. This is because the performance of an inductive link depends on the mutual coupling between coils, which reduces drastically as the distance increases. To achieve high power transfer efficiency (PTE) in powering miniaturized implants with mm-sized coils, the operation frequency (f_c) should be increased to several hundreds of MHz or even GHz [7]-[10]. But utilizing such high frequencies significantly reduces the maximum allowable transmitted power under the specific absorption rate (SAR) constraints [11].

The most attractive modality for WPT to miniaturized devices implanted in deep tissues is US. In a typical US WPT link, an external US transducer (coupled to the skin) generates US waves in the medium, which are received by a small US transducer in the implant and converted to an AC voltage. Compared to electromagnetic waves, US waves enjoy low acoustic loss in tissue [12], small wavelength even at MHz-range frequencies (critical for focusing) due to the low US speed in tissue, and a high FDA safety limit [13]. These features have collectively held the promise of efficient and safe US WPT to mm-sized implants at cm-scale depth [14].

Over the past decade, several groups have presented US links for WPT in different applications, such as neural/gastric-wave recording, electrical/optical stimulation, and pressure/temperature sensing, to name a few [15]-[27]. For example, US WPT links have been demonstrated in [18] and [19] for powering a 30.5 mm^3 pressure sensor at 12 mm distance and a 1.7 mm^3 stimulator at 70 mm distance, respectively. We have also demonstrated a US WPT link for gastric-wave recording, achieving a PTE of 0.52% in delivering 0.17 mW to a 1.1 mm^3 receiver (Rx) at ~ 38 mm distance [16].

The current literature has mostly focused on designing and optimizing mm-sized US transducers as the implanted Rx in US WPT links. A single commercially available or custom-made US transducer has been used as the external transmitter (Tx). For instance, a systematic design approach for finding the optimal geometry and f_c of the piezoelectric Rx to maximize the backscatter bandwidth and modulation depth has been proposed in [27]. We have also presented the design and optimization of custom-made disc-shaped piezoelectric transducers and f_c for US WPT. We have reported a measured PTE of 0.65% at f_c = 1.1 MHz for WPT to a 1 mm^3 Rx at 30 mm distance from a disc-shaped piezoelectric Tx [25].

To compensate for implant's misalignment and/or power a network of mm-sized implants, several works have recently demonstrated US arrays with the capability of steering focused US beams. In [28], a 3.8×3.8×0.5 mm^3 sectored-multiring US transducer has been developed for selective powering of brain implants at 1–3 mm distance (f_c = 2.9 MHz) within a small area (~ 2.3 mm^2). In [29], the performance of a spherically focused US transducer has been compared with that of two rectangular 2D arrays only in simulations. A 1.1 MHz, 32-element linear (1D) US phased array has been developed in [30] to demonstrate various beam patterns in a tissue phantom. In [31], a 52-element 2D array made with 0.8 mm diced PZT cubes (f_c = 1.5 MHz) has been demonstrated to deliver 13 μW to a ~ 0.5 mm^3 Rx at 50 mm distance with a PTE of ~ 0.018% using ± 5 V pulses across the array. A 40 kHz, 37-element array for through-air WPT to a large Rx with 11 mm diameter has been fabricated in [32], achieving a measured PTE of 4% at 50 mm distance in air. Finally, a 676-element 2D array (5×4 mm^2) integrated on a 5 V CMOS chip has been demonstrated at f_c = 8.4 MHz in [33], achieving up to 100 kPa of US pressure output at 5 mm distance.

Although several US arrays for WPT have been presented, the literature still lacks a detailed design methodology for simultaneously finding the optimal geometries of the Tx phased array and Rx transducer in Fig. 1, as well as the optimal f_c to achieve the highest PTE. In other words, in prior works either a single US transducer has been used as Tx or the US array has not been optimized based on a meticulous design methodology that considers both the application and fabrication constraints for optimal US WPT with beam focusing and steering at different depths and angles.

The main contributions of this paper are: 1) Presenting an optimal design methodology of US WPT links operating with a phased array Tx using an iterative design procedure with low computational expense that maximizes PTE by optimizing the geometries of Tx array and Rx transducer as well as f_c for given application and fabrication constraints; 2) Proposing a new figure of merit (FoM) that improves the power efficiency of the US array and enables its optimization in a computationally inexpensive tool; 3) Helping the designers of US WPT systems optimize a US phased array for WPT to an implant, experiencing large misalignments, and/or to a network of implants; And 4) validating the proposed design procedure with comprehensive experimental results.

The theoretical foundation of US beam steering and focusing will be discussed in Section II, followed by the design and optimization of US WPT links with phased arrays for mm-sized implants in Section III. The fabrication and measurement results of the optimized design will be presented in Section IV, followed by the discussions and concluding remarks in Sections V and VI, respectively.

II. Theory of Wireless Power Transfer with Ultrasonic Beam Steering and Focusing

We have already described the theory of US WPT with a pair of disc-shaped US transducers in [25]. The PTE of a US WPT link depends on the acoustic intensity of the transmitted beam I_o (through Tx in Fig. 1) at the Rx location, Rx effective cross-section area A_2, and the

mechanical-electrical power conversion efficiency (PCE) of Rx (η_2). The link PTE can be found from,

$$PTE = I_o \times A_2 \times \eta_2 / P_{in} \quad (1)$$

where P_{in} is the delivered electrical power to Tx from the energy source. Note that the PCE of Tx (η_1) is already included in I_o, and the US pressure (proportional to I_o) is assumed to be constant within A_2 in formulating (1).

While a disc-shaped transducer (similar to [25]) is also used as Rx in this work, this paper is focused on designing US WPT links with a phased array as Tx. Thus, it is critical to understand the theoretical foundation of US beam steering and focusing with a phased array. While the basic theory has been studied in the literature [34], [35], a summary with an emphasis on key parameters in the WPT context is given here. For simplicity, this paper optimizes and characterizes linear (1D) phased arrays, but similar design methodologies can also be generalized to 2D phased arrays.

A. Design Parameters for Ultrasonic Phased Array (Power Transmitter)

A linear phased array consists of several US transducer elements arranged in a single line assembly with identical spacing. As an example, Fig. 2 shows a linear phased array with 8 elements ($N = 8$), in which d is the interelement spacing (or pitch), a is the element width, L is the element length in the elevation direction, and D is the total array width (or aperture). The difference between d and a is the *kerf*. The thickness of each US element is denoted by t. Thus, the geometric design parameters of a linear US phased array are d, L, a, N, D, and t. In this paper, the top surface of the array is assumed to be in the $\boldsymbol{yz}$ plane (centered at the origin), having its aperture and elevation length extending along the $\boldsymbol{y}$ and $\boldsymbol{z}$ axes, respectively.

The US beam generated by a linear array, while driving all its elements with the same phase, has two distinct zones: Fresnel zone (near field) and Fraunhofer zone (far-field) [36]. A linear array can only be focused within the near-field region, which ends at the Rayleigh distance, $Z_{TR} = D^2/4\lambda$ ($D >> \lambda$), where λ is the US wavelength in the medium [12].

For beam formation at a particular focal depth (F), the US elements should be excited with a specific delay pattern so that US waves from all the elements arrive at F constructively (with the same phase). For optimal beam steering and focusing at F with the azimuthal angle θ_s (in the $\boldsymbol{xy}$ plane with respect to the normal axis $\boldsymbol{x}$ in Fig. 2), the excitation time delay (Δt_n) for the n^{th} element can be calculated from:

$$\Delta t_n = (F/c)\left(1 - \sqrt{\left[1 + (nd/F)^2 - 2nd\sin(\theta_s)/F\right]}\right) \quad (2)$$

where $c = \lambda \times f_c$ is the US velocity [34]. In addition to the main lobe in the steering direction θ_s, there are also side lobes in many other directions and grating lobes whose magnitudes are comparable to the main lobe.

The effect of US array parameters on its beam steering and focusing capability has been studied in [35] with some simplifications. They have defined a directivity function, $H(\theta)$, as the peak US pressure at any angle θ normalized by the peak US pressure at the steering angle θ_s:

$$H(\theta) = \left| \frac{\sin[\pi a \sin(\theta)/\lambda]}{\pi a \sin(\theta)/\lambda} \frac{\sin[(\pi d(\sin(\theta_S) - \sin(\theta))/\lambda)N]}{N \sin[(\pi d(\sin(\theta_S) - \sin(\theta))/\lambda)]} \right| \quad (3)$$

Note that $H(\theta) = 1$ at $\theta = \theta_s$, and it depends on the array geometry (a, d, N). To attenuate side/grating lobes, $H(\theta)$ should be minimized at $\theta \neq \theta_s$. Based on (3), the array directivity improves by increasing both N and d (or D), but increasing θ_s degrades the directivity. While increasing N (or D) improves the directivity, it has been shown in [35] that the directivity improvement is relatively less at very large N.

At large d with improved directivity, amplified side/grating lobes may be introduced. By simplifying the array to discrete line sources, the maximum d that avoids grating lobes for a given θ_s has been found in [35]:

$$d_{max} = \lambda/(1 + \sin\theta_S) \times (N - 1)/N \quad (4)$$

Therefore, d cannot be increased indefinitely. For example, with large N and $\theta_s = 90°$, d_{max} becomes $\lambda/2$.

In optimizing WPT links, maximizing the link PTE in (1) is the main goal. Therefore, while small side/grating lobes are preferred, this should not be achieved at the cost of reducing PTE of the US WPT link. Indeed, the US pressure (or I_o) at the focal spot (where Rx locates) should be increased to optimize PTE. Therefore, considering the complexity of a US WPT link, an accurate design methodology with low computational expense is needed to optimize the geometry of a US phased array (d, L, a, N, D, t) for WPT to mm-sized implants given the realistic application and fabrication constraints.

B. Design Parameters for Ultrasonic Receiver

Due to limitations on the Rx size in mm-sized implants, its transducer diameter (D_{Rx}) and thickness (t_{RX}) should be limited to mm dimensions and below. In [25], we have provided a detailed study on the effect of D_{Rx} and t_{Rx} on the performance of a mm-sized US Rx in a WPT link, which is not repeated here for the sake of brevity. It was shown in [25] that considering impedance matching, acoustic diffraction, and f_c, both D_{Rx} and t_{Rx} need to be swept in a finite-element-method (FEM) simulation to optimize PTE.

III. Optimal Design of Ultrasonic Wireless Power Transfer Links With Phased Arrays

The geometric design parameters of a US WPT link are L, a, N, D, and t of the Tx US array and D_{Rx} and t_{Rx} of the Rx US transducer. For WPT to mm-sized implants, f_c and targeted tissue dictating the maximum F and θ_s as well as c (or λ) are among the design parameters. Optimizing these parameters is critical for achieving the highest PTE. Since the

size of each US transducer is relatively small, (1)–(3) in [25] and (1)–(4) in this paper can be used to find the initial values for these parameters. But further optimization is needed in accurate simulation tools, such as COMSOL Multiphysics (COMSOL, Burlington, MA) and the k-Wave toolbox in MATLAB (MathWorks R2019b, Natick, MA).

The optimal D_{Rx}, t_{R_x}, and f_c (and t of the array) are found with COMSOL simulations, following the procedure that has been described in detail in our previous work [25]. Due to the complexity of a US phased array, its optimization in COMSOL is very challenging. The COMSOL models of large arrays with high-frequency transducers suffer from long simulation times and high computational expense. Thus, for optimizing the array geometry (d, L, a, N, D), k-Wave is used. The resultant acoustic field radiated from multiple sources can numerically be calculated in k-Wave by solving a set of coupled first-order wave equations [37]. The k-Wave accuracy has experimentally been validated [38].

Fig. 3 shows our US array setup in k-Wave, in which a 660×512×256 grid space with a pixel resolution of 61 μm is defined for a maximum frequency of ~ 8.4 MHz. The array surface is parallel to the ***yz*** plane and centered at the origin (***x*** = ***y*** = ***z*** = 0). The ***xy*** and ***xz*** planes with 660×512 and 660×256 grid points are defined as sensors for recording US pressure output. The grid space is defined such that the first 15 ***yz*** planes (thickness of ~ 0.9 mm) from the array surface and beyond that (645 planes) have acoustic properties of sylgard-184 (Dow Inc., Midland, MI) and soft tissue, respectively (in measurements, the array was coated with sylgard-184). The temporal acoustic wave propagation is simulated for ~ 34 μs with 2751 steps of ~ 12.3 ns. To model the boundary condition and avoid US reflections, a 0.64 mm thick perfect matching layer (PML), which is a perfect US absorber, is added at the boundaries of the medium in k-Wave simulations. The sound speed in (and mass density of) soft tissue and sylgard-184 are set to 1540 m/s (1060 kg/m^3) and 1030 m/s (1050 kg/m^3), respectively [39], [40]. An acoustic loss coefficient of 0.75 dB/MHz/cm is considered in k-Wave.

A. Design Procedure of Optimizing US WPT Links with Phased Arrays for Powering mm-Sized Implants

A design procedure is presented in Fig. 4 to maximize the PTE of a US link with an array for WPT to mm-sized implants by optimizing f_c and the geometries of the Tx array and Rx transducer. The proposed optimization flowchart in Fig. 4 has two parts. First, the geometry of the mm-sized Rx transducer (D_{Rx}, t_{R_x}) and f_c are optimized in COMSOL using our design procedure in [25] by simplifying the US array with a disc-shaped transducer with a natural focus. In this step, the PCE of the Rx transducer, i.e., η_2 in (1), is optimized to maximize PTE. Then, the array geometry (d, L, a, N, D) is optimized in k-Wave. The thickness of each US element (t) in the array is also optimized in COMSOL to resonate them at the optimal f_c

The Rx geometry and f_c are optimized to maximize PTE. In COMSOL, a source drives the Tx transducer, and a load is connected to the Rx transducer. Then the input and output power is calculated to find PTE in each simulation. For optimizing the array, defining PTE

in k-Wave is not trivial as k-Wave operates based on US pressure fields. For optimizing phased arrays for US WPT, a new FoM is proposed as:

$$FoM = \int_{SF \times \mathrm{A2}} (P/\sqrt{N \times a \times L})^2 \cdot dA = \left[\int_{SF \times \mathrm{A2}} P^2 \cdot dA\right] / (N \times a \times L) \approx P^2 \times SF \times A_2/(N \times a \times L) \quad (5)$$

where P is the spatial peak US pressure at the focal spot and SF is a safety factor (explained later).

As the pressure source of each element is defined with uniformly distributed point sources over a defined source mask in k-Wave, by increasing $N{\times}a{\times}L$, which is the total piezoelectric area, the input electrical power to the array is also increased. Since the US pressure squared (P^2), which is related to I_0 in (1), is proportional to the input power, the term $P/\sqrt{NaL}$ is considered in the FoM to ensure a constant total input power to the array as N, a, and L are swept in the optimization. Therefore, this FoM optimizes the power efficiency of the array (and thereby the whole link) by maximizing the received power by the Rx transducer (proportional to $I_0{\times}A_2$ and thereby $P^2{\times}A_2$) at a constant input power, i.e., constant P_{in} in (1). It is worth noting that k-Wave simulations cannot consider t. Therefore, t is not considered in FoM and should be optimized in COMSOL as the last step. Since the input power is maintained constant in k-Wave simulations with the proposed FoM, sweeping t, which changes the elements' impedance, implies that a different voltage is required across each element to achieve the desired input power. In other words, t needs to be swept based on optimal f_c only once at the last step, and its optimization does not need to be iterated.

Maximizing FoM for a constant input power in (5) implies optimizing PTE in (1) because P^2 is proportional to I_o, and its integration at the implant's location over $SF{\times}A_2$ area relates to the received power by the Rx transducer. If the pressure distribution is uniform over $SF{\times}A_2$ area, the integral can be simplified as shown in (5). However, for accurately calculating FoM in k-Wave, the discrete integration tool is used over a designated area (represented by a 2D matrix) on the ***yz*** plane in Fig. 3 (where the implant locates).

Depending on the application, a mm-sized implant can experience small or large displacements in practice. For small movements comparable to λ, the safety factor SF is considered to ensure maximum power delivery within a small displacement range of $SF{\times}A_2$. For large movements (or powering a network of implants), an image-guided method similar to [31], [41], and [42] is needed to refocus the US beam toward the implant (or different implants). While this is not the focus of this paper, the capability of the array in beam steering in worst-case scenarios should still be considered in the optimization. Since the US pressure (P) at the focal spot reduces as θ_s increases, the ratio of P at $\theta_{s,max}$ to P at $\theta_s = 0$, i.e., $P_{\theta_{s,max}}/P_0$, should be considered in the optimization. To achieve at least half of the US intensity (or power) at $\theta_{s,max}$, compared to that of $\theta_s = 0$, $P_{\theta_{s,max}}/P_0 > 0.7$ should be considered along with FoM optimization.

The optimization flowchart in Fig. 4 starts with the design constraints imposed by the application and driving electronics, including 1) the maximum Rx size, constraining D_{Rx}

and t_{Rx}, 2) the nominal values for the powering distance F (or focal depth) and load resistance R_L, 3) sound speed (c) in the targeted tissue, 4) maximum powering distance (F_{max}) and steering angle ($\theta_{s,max}$), considering the expected displacements of the implant and/or the worst-case scenario in WPT to a network of implants, 5) maximum allowable array size (D_{max} and L_{max}), and possibly 6) the maximum number of elements (N_{max}) and maximum delay range ($\Delta t_{n,max}$), limited by driving electronics. Also, design constraints imposed by the fabrication limitations, such as the minimum *kerf* limited by the blade thickness of a saw machine, are included in step 1.

One should note that some of these parameters are related as $a \leq d - kerf$, $\lambda = c/f_c$, and $N \times d - kerf = D$. Therefore, they can affect each other in the optimization. Also, to achieve beamforming at worst-case F_{max}, a minimum D (and N) is required based on $F < D^2/4\lambda$ criteria (i.e., $D_{min} = \sqrt{F_{max} \times 4\lambda}$ To achieve the most optimal design, we recommend that the array geometry is optimized based on D limitations (not N_{max} from electronics), from which driving electronics can then be developed with optimal N channels. Also, since the largest delay is need for steering at $\theta_{s,max}$, the $\Delta t_{n,max}$ limitation of the driver can affect the range for d as formulated in (2).

In step 2, the initial values for f_c, d, a, D, and N are chosen. The following guidelines can be used for selecting these parameters. 1) The initial value for f_c can be found based on the guidelines in [25]. 2) Based on (4), $d = \lambda/2$ is chosen as the initial value to minimize side/grating lobes at large θ_s. 3) The large $a = \lambda/2 - kerf$ is chosen as the initial value for a to provide more US pressure. 4) Based on (3), to improve the array directivity N_{max} is chosen as the initial value as long as $N_{max} \times \lambda/2 - kerf \leq D_{max}$. If this condition is not satisfied or N_{max} is not imposed by the design, D_{max} is chosen as the initial value for D, and initial N can be found from $N \times \lambda/2 - kerf = D_{max}$. If D_{max} is not imposed by the application either, D_{min} is chosen as an initial value, from which initial N is found.

The geometry of the Rx transducer (D_{Rx} and t_{Rx}) and f_c are optimized in step 3 to maximize PTE based on our design procedure in [25] (the US array is simplified with a disc-shaped transducer). This provides optimal D_{Rx} (or A_2), t_{Rx}, and f_c, which will be used to optimize the array in the next steps.

In step 4, the geometry of the US array (L, a, d, D, N) are optimized in k-Wave to maximize the FoM in (5) at nominal F ($\theta_s = 0$) and achieve $P_{\theta_{s,max}}/P_0 > 0.7$ at given $\theta_{s,max}$. First, L is swept in step 4.1, and the value of L that maximizes FoM with $P_{\theta_{s,max}}/P_0 > 0.7$ is chosen. In step 4.2, d and a ($a \leq d - kerf$) are swept to maximize FoM with $P_{\theta_{s,max}}/P_0 > 0.7$ using the value for L from step 4.1. The following constraints are considered in this step. 1) If D_{max} is given by the application, N should also be changed in step 4.2 to achieve $N \times d - kerf = D_{max}$ at each d as long as $N \leq N_{max}$ (if imposed by the design). 2) If only N_{max} is given, $N = N_{max}$ at each d. 3) If neither D_{max} nor N_{max} are given, N should also be changed in step 4.2 to achieve $N \times d - kerf = D_{min}$ at each d. This step leads to a 3D surface for FoM vs. d and a, and the values of d and a that maximize FoM are chosen as long as $P_{\theta_{s,max}}/P_0 > 0.7$.

Using the values for d and a from step 4.2, then N is swept in step 4.3 with the constraint of $D_{min} \leq N \times d - kerf \leq D_{max}$ and $N \leq N_{max}$, and the value of N that maximizes FoM with $P_{\theta_{s,max}}/P_0 > 0.7$ is chosen. Steps 4.1–4.3 are repeated iteratively until d, a, and N change less than 1% in step 4.4. After each iteration, the optimal N in step 4.3 is fixed for sweeping L, d, and a in steps 4.1 and 4.3. This leads to optimal US array and Rx transducer geometries for the optimal f_c.

In step 5, a single US element is modeled in COMSOL using the optimized a and L from k-Wave, and t is swept to resonate the element at the optimal f_c. The resonance frequency of a piezoelectric transducer is inversely proportional to its dimension [25]. Defining the element aspect ratio $AR = a/t$, it is established in [43] that for $AR >> 1$ or $AR << 1$, the thickness-mode resonance frequency is the most efficient one to drive a piezoelectric transducer. In these conditions, the thickness-mode resonance can easily be tracked as t is swept in COMSOL simulations, and the t value that sets the thickness-mode parallel resonance at the optimal f_c is chosen. But when AR is close to one, thickness and width resonance modes are highly coupled, showing two nearby resonances in COMSOL simulations. In this case, our measurements of US elements with different AR values close to one showed that the first resonance is more efficient and should be set at f_c.

Step 5 determines the most optimal values for the geometry of the US transducers and array as well as f_c to achieve the highest PTE, which can further be validated and fine-tuned through measurements. It is worth noting that our optimization process makes some simplifications in finding optimal f_c by approximating the Tx array with a disc-shaped transducer in step 3 to drastically reduce the computational expense. Therefore, further fine optimization of f_c can be considered in measurements as will be discussed in Section IV.B.

B. Design Example of US WPT Link with Phased Array for mm-Sized Implants

Based on the design procedure in Fig. 4, a US link with a phased array was optimized for WPT to a mm-sized implant with high PTE. For the design example, the following assumptions were made: 1) piezoelectric transducers were made of PZT-5A (APC International, Mackeyville, PA), 2) Rx was constrained within 1 mm^3 and its US transducer was mounted on a silicon die (mimicking implant's circuitry) with 0.3 mm thickness, which limited the disk-shaped Rx geometry to $D_{Rx,max} = 1.2$ mm and $t_{Rx,max} = 0.7$ mm, 3) Rx was located at $F = 30$ mm inside soft tissue with $c = 1474$ m/s, 4) SF of 1.5 to compensate for implant's small displacements, and F_{max} of 30 mm and $\theta_{s,max}$ of ±45 for large movements, 5) D_{max} and L_{max} of 26 mm to limit the size of the array, and 6) the link was designed to deliver mW power levels (R_L of ~ 2.5 kΩ).

To demonstrate a US WPT link as the proof of concept, PZT-5A with the material properties of $d_{33} = 400$ pC/N, density of 7600 kg/m^3, acoustic impedance of 31.5 Mrayl, and Curie temperature of 360 °C was used. In general, PZT-5A provides high electromechanical coupling coefficient, which is key in maximizing PTE, and also has high resistivity at elevated temperatures. The same design procedure can also be applied to US transducers with different piezoelectric materials such as PZT-5H, which has even higher d_{33} but lower Curie temperature.

Table I summarizes the optimization results for the design example (designated as optimal-design link) by following the procedure in Fig. 4. The geometry of the Rx (D_{Rx}, t_{Rx}) and f_c were first optimized in COMSOL to maximize PTE based on [25]. It was then followed by optimizing the Tx array geometry in k-Wave (except t) to maximize FoM in (5) at F = 30 mm and achieve $P_{\theta_{s,max}}/P_0 \geq 0.7$ at $\theta_{s,max}$ = 45°.

Fig. 5a illustrates the normalized FoM vs. L for N = 48, $d = \lambda/2$ = 0.55 mm, a = 0.49 mm, and $kerf$ = 61 μm at F = 30 mm and θ_s = 0°. The optimum L is 7.33 mm, using which the normalized FoM vs. a and d for constant D of 26 mm (N is changed for each d) is shown in Fig. 5b. In these simulations, as d and a were increased, the FoM also increased. However, as shown in Fig. 5c, illustrating $P_{\theta_{s,max}}/P_0$ at $\theta_{s,max}$ = 45° for each d (using a values that corresponded to maximum FoM in Fig. 5b), $P_{\theta_{s,max}}/P_0$ reduced as d was increased. To simultaneously maximize FoM and achieve $P_{\theta_{s,max}}/P_0 \geq 0.7$ at $\theta_{s,max}$ = 45°, optimum d and a of 0.55 mm and 0.49 mm were selected, respectively. Fig. 5d shows how normalized FoM changes with N even beyond optimal N of 48, which corresponds to D of 26 mm. By increasing N, the FoM initially improved and then started to saturate and decrease for $N \geq$ 48.

Finally, Fig. 5e shows the simulated (COMSOL) impedance profiles of one US element (L = 7.3 mm, a = 0.49 mm) vs. frequency at different t (related to different aspect ratios AR). By changing AR from 0.17 to 4, the resonance frequency shifted from ~ 0.6 MHz to ~ 3.5 MHz. The optimal f_c of 1.4 MHz was achieved at AR of 0.36 (t = 1.34 mm).

Fig. 6 shows the simulated beam profiles of the optimal array in ***xy*** and ***yz*** planes when the beam was focused at F = 30 mm and θ_s = 0° (f_c = 1.4 MHz). The normalized peak pressure values in the ***xy*** and ***yz*** planes were 1 and 0.97, respectively. The half-power beam width (HPBW), at which the US intensity reduces to half (−3 dB) or US pressure reduces by ~ 1.4-fold, at the focal spot in ***x***, ***y***, and ***z*** directions was 9.4 mm, 1.2 mm, and 3.9 mm, respectively.

IV. Ultrasonic WPT Link Fabrication and Characterization

In this paper, the commercially available TX7316EVM evaluation board (Texas Instruments, Dallas, TX) with 16 channels of high-voltage drivers (up to 200 V) and a delay range of 0–40 μs (5 ns resolution) was used for driving the array in measurements. Therefore, considering the limited number of channels (i.e., N_{max} = 16) and other fabrication constraints, such as $kerf$ of 150 um based on the available blade thickness, the design procedure in Fig. 4 was used to optimize a US WPT link for measurement purposes, which is designated by “Meas. Link” in Table I. To achieve optimal beamforming with limited N at $\theta_{s,max}$ of ±45°, F was reduced to 20 mm. Our measurements in [25] showed optimal f_c = 1.1 MHz and $R_{L,PTE}$ = 850 Ω after fabricating the mm-sized Rx transducer. Therefore, these values were used to optimize the array for measurement purposes to simultaneously maximize FoM and achieve $P_{\theta_{s,max}}/P_0 \geq 0.7$ at $\theta_{s,max}$ = 45°. It is worth noting that our measurement results in this section are mainly aimed at demonstrating the accuracy of

k-Wave simulations, which are used to optimize the array, and an exemplary US WPT link with a Tx phased array.

A. Fabrication of Ultrasonic WPT Link

Fig. 7a shows the fabrication procedure of the linear US array. A printed-circuit board (PCB) was first designed and fabricated with 16 excitation pads with 0.7 mm spacing and one large ground pad (two dummy pads/elements were added on the sides to consider fabrication imperfections). A disc-shaped PZT-5A was cut to a rectangular shape with optimal array aperture and length. It was glued to the PCB using conductive silver paint (Leitsilber 200, Ted Pella Inc., Redding, CA) for electrical connection and an epoxy adhesive for mechanical reinforcement during dicing. An ADT700 dicer machine with a saw blade of ~ 150 μm thick was used to dice the PZT plate to provide 16 elements (discarding two dummy elements on the sides) with 0.49 mm width. A carbon tape was used to stick the PCB to a holder by heating it up to 60 °C. After dicing the sample, a dual-row 20-pin header connector was soldered to the PCB for connecting the array to the driving electronics with a cable.

The top plate of each US element was wire-bonded to its corresponding excitation pad on the PCB. To ensure proper electrical connection on both top and bottom plates with wire-bonds and silver epoxy, S-parameter measurements were conducted using a network analyzer to find the impedance profile of each element. Finally, a layer of sylgard-184 was coated on the array for electrical isolation and protection of wire-bonds inside a water tank. In k-Wave simulations, introducing a 0.9 mm thick sylgard-184 layer reduced the US pressure output of the array by ~ 16% at $F = 20$ mm ($\theta_s = 0°$).

As shown in Fig. 7b, similar to [25] the Rx US transducer was mounted on a small PCB with ~ 7×7 mm^2 area and 1.5 mm thickness. To minimize undesired interconnect effects, transducer's top plate was wire-bonded to the PCB pad, while its bottom plate was connected to the PCB ground pad using conductive epoxy. The transducer was connected to an SMA connecter using AWG28 magnet wire. The assembled device was coated with a layer of sylgard-184.

B. Measurement Results

Fig. 8a shows the block diagram of the TX7316EVM evaluation board for driving the US array in our measurements. The key component on this board is the TX7316 chip that includes 16-channel 3-level pulser circuits, active transmit/receiver switches, and integrated transmit beamformer. The board includes a complex programmable logic device (CPLD), which is connected to the PC via a USB cable. Through a graphical user interface (GUI), the chip is configured with optimal parameters, such as the pattern and delay profiles. The board provides both on-chip and off-chip beamforming modes. In the on-chip beamformer mode, which requires less control signals and is used in this work, the delay profile for the pulsing of the different channels is stored on chip. The chip supports a beamformer delay resolution of one high-frequency clock period and a range of 2^{13} clock periods. An internal pattern generator generates the output pulse patterns based on pattern profiles stored in a profile RAM. The TX7316EVM board was used to drive the array without any external electrical matching network.

Fig. 8b shows the measurement setup for characterizing the US WPT link, including the fabricated US array and Rx transducer inside a water tank. In some of our measurements, the US array was wrapped in a 3 mm thick layer of chicken breast to mimic the lossy tissue environment. The TX7316EVM board was powered by a DC supply as high as 150 V with 30 mA limited current. The driver board was controlled by an application programming interface in a PC, and it was programmed to generate 6 pulses (spaced by $1/f_c$) repeated with a 1 ms interval delay. A sync pulse generated by the board was used as the trigger to collect measured data.

For US pressure measurements, the calibrated HGL0085 hydrophone (Onda Corp., Sunnyvale, CA) connected to a digital oscilloscope (with 50 Ω termination) via the Onda AG-2010 preamplifier (providing ~ 20 dB voltage gain) was used. The HGL0085 with 0.25–40 MHz bandwidth, 85 μm aperture, and pressure sensitivity of 49.1 nV/Pa at 1.1 MHz has a good directivity response, collecting > 80% of the generated US pressure at < 45° angles. For US beam profile measurements with axial and lateral scanning, a custom 3-axis translational stage with three motorized linear stages (moving range of 5 cm and resolution of 0.8 μm) was used, similar to [44]. In all measurements, the array was fixed while a PC controlled the position of the hydrophone (or Rx transducer).

Using a network analyzer, the impedance profiles of all the 16 elements in the fabricated array and the Rx transducer were measured. Fig. 9a shows the impedance of 16 US elements in the frequency range of 0.6–1.6 MHz, in which resonance and anti-resonance modes with kΩ-range impedance can be observed. Fig. 9b shows the Rx transducer impedance of 1.3 kΩ and 2.6 kΩ at resonance (1.1 MHz) and anti-resonance (1.27 MHz) modes, respectively.

In the following, a method is proposed to find tune f_c for driving the array to achieve the highest US pressure output with minimal input electrical power (i.e., high power efficiency in the array). First, as shown in Fig. 10a, the peak US pressure output of each element (driven with 20 V peak-peak sinusoids at different frequencies) was measured at $F = 20$ mm along the axial distance ($\boldsymbol{x}$ axis in Fig. 3) while aligning the hydrophone with individual elements. Then, the input power of each element was measured under the same conditions (Fig. 10b). From Figs. 10a and 10b, it is clear that relatively high US pressure output can be achieved at the 1–1.2 MHz frequency range with much smaller input power compared with the frequency range of 0.8–1 MHz. For instance, although the averaged (of 16 elements) peak US pressure output at 0.84 MHz was ~ 10% higher than the averaged pressure at 1.1 MHz (4.5 kPa vs. 4.1 kPa), the averaged input power at 0.84 MHz was 3.3-fold higher (22 mW vs. 6.6 mW). Therefore, f_c= 1.1 MHz was chosen as the operation frequency (also considering the frequency response of Rx transducer), aligned with our optimized design.

The results in Figs. 9 and 10 show that the PZT element is more power efficient at frequencies close to anti-resonance as opposed to resonance. The mechanical quality (Q_m) factors play a significant role in losses of piezoelectric resonators, which include dielectric, elastic, and piezoelectric losses, where a higher Q_m increases the power efficiency. Due to the significantly large piezoelectric loss compared to dielectric and elastic losses in PZTs, it is established that the anti-resonance Q_m is larger than the resonance Q_m (e.g., in both k_{31} and k_{33} modes) [45]. Therefore, as also observed in our measurements in Fig. 10, the

anti-resonance operation requires less power than the resonance mode for generating the same vibration velocity, i.e., the anti-resonance mode achieves higher efficiency.

For beam steering and focusing at different depths (F) and angles (θ_s), the TX7316EVM board was programmed with optimal delays obtained from k-Wave simulations. As an example, Figs. 11a and 11b show the delay patterns for beamforming at different F of 10–30 mm ($\theta_s = 0°$) and θ_s of 0–60° ($F = 20$ mm), respectively. Fig. 11 clearly illustrates that the closer an element is to the focal spot, the larger its delay is.

Figs. 12a and 12b show the measured transient waveforms of the TX7316EVM driver across 4 US elements (# 2, 5, 12, 15 in Fig. 7) for beamforming at $F = 20$ mm with $\theta_s = 0°$ and 45°, respectively, using the delays in Fig. 11. Fig. 12c shows the typical transient waveforms of the burst-mode signals generated by the driver, including the 6 excitation pulses of one channel, as well as the received voltage by the Rx transducer ($F = 20$ mm, $\theta_s = 0°$).

Using the hydrophone, the beam profile (US pressure output) generated by the 16-element phased array was measured in the ***xy*** plane (Fig. 3) with 200 μm resolution in the water tank. Fig. 13 compares the simulated and measured beam profiles when the beam was focused at $F = 20$ mm and steered with $\theta_s = 0$ °, 45 °, and −45 ° (the array was driven with 100 V pulses). The measured peak pressure and axial and lateral HPBW at the focal spot were 0.83 MPa, 18.8 mm, and 2 mm at $\theta_s = 0°$, respectively. The measured US pressure output reduced to 0.57 MPa and 0.42 MPa at θ_s of 45° and −45°, respectively. The simulated axial and lateral HPBW were 20 mm and 2 mm at $\theta_s = 0°$, which are close to the measurement results. For fair comparison, water was also used as the medium for these simulations ($c = 1482.3$ m/s, mass density = 1000 kg/m^3, loss coefficient = 0.002 dB/MHz/cm). The simulated values for US pressure in Fig. 13 (and Fig. 14) are all normalized to the peak US pressure at $F = 20$ mm and $\theta_s = 0°$ in the water medium (Fig. 13a).

As it can be seen from Figs. 13b and 13c, there is some discrepancy between the simulated and measured axial HPBW at θ_s of ±45° (and smaller US pressure compared to Fig. 13a) that could potentially be due to the small size of the array ($N = 16$), with which beam steering at large angles is challenging. The smaller US pressure at $\theta_s = ±45°$ is partly due to the directivity of the hydrophone, which can receive 80% of the US pressure at ±45° angles.

To characterize the effect of tissue, the beam profile generated by the phased array at $F = 20$ mm and $\theta_s = 0$ ° was also simulated and measured in the presence of the chicken breast in the water tank, as shown in the Fig. 8 inset. Fig. 14 shows the measured peak pressure and axial and lateral HPBW of 0.8 MPa, 18.5 mm, and 1.9 mm at the focal spot, respectively, which are very close to those without chicken in Fig. 13a. Therefore, the chicken tissue had minimal effect.

When the beam was focused at $F = 20$ mm ($\theta_s = 0°$) by driving the array with pulses with optimal delays and different amplitudes of 10–150 V, the received power (P_L) by the 1 mm^3 Rx transducer was measured at different loading conditions (R_L), as shown in Fig. 15. The US WPT link delivered optimal P_L of 0.037 mW to 12.6 mW (with 10–150 V pulses) to the 1 mm^3 Rx at a depth of 18 mm (slightly smaller than F of 20 mm) using an optimal R_L of 850 Ω in all conditions.

The PTE of the US WPT link (excluding driver efficiency) was also characterized by measuring the input power to each US element of the array and P_L of the Rx transducer when the beam was focused at F = 20 mm (θ_s = 0°). Fig. 16 shows the measured link PTE at different R_L at the axial distance of 18 mm (where P_L was maximum). In these conditions, the highest PTE of 0.14% was achieved at R_L = 850 Ω. As expected, the link PTE remained fairly constant at different voltage levels across the array.

To further characterize the US WPT link, P_L was measured with optimal R_L of 850 Ω when the beam was focused at different depths (F of 10–30 mm; θ_s = 0°) and angles (θ_s of 0–60°; F = 20 mm) with 100 V pulses across the array. In each measurement with a specific F and θ_s, the optimal delay pattern was found from the k-Wave simulations. Fig. 17 shows the results of these measurements in the water tank without and with the chicken breast.

Figs. 17a and 17b show the measured P_L in axial $\boldsymbol{x}$ ($\boldsymbol{y}$ = $\boldsymbol{z}$ = 0) and lateral $\boldsymbol{y}$ ($\boldsymbol{z}$ = 0, $\boldsymbol{x}$ = corresponding to highest P_L) directions, respectively, when the beam was focused at F of 10–30 mm (θ_s = 0°). Fig. 17a shows that as F was increased from 10 mm to 30 mm, the location of the peak P_L moved to larger depths, while the peak P_L (and PTE) reduced from 7.3 mW (and 0.173%) to 4.9 mW (and 0.12%). Since N was limited to 16 in the fabricated array, the maximum P_L occurred at locations smaller than F, particularly at $F \geq$ 20 mm, implying the need for a larger array with higher N. Fig. 17b shows a similar phenomenon and that the lateral HPBW is almost the same as F changes.

Figs. 17c and 17d show the measured P_L in axial and lateral directions, respectively, when the beam was focused at F = 20 mm with different θ_s of 0–60°. In Fig. 17c, for each θ_s measurement Rx moved in parallel with $\boldsymbol{x}$ around its corresponding focal spot ($\boldsymbol{z}$ = 0 but different $\boldsymbol{y}$). In Fig. 17d, Rx was located at the axial distances that resulted in peak P_L for each F in Fig. 17a. It can be clearly seen that the peak P_L reduced as θ_s increased. For instance, increasing θ_s from 0° to 60° reduced peak P_L from 6.1 mW to 0.24 mW. This could be due to two reasons. 1) As also shown in Fig. 13, the peak US pressure reduced by 31.3% at θ_s = 45° compared to that of θ_s = 0° (0.57 MPa vs. 0.83 MPa). This can potentially result in ~ 2-fold reduction in P_L and can be mitigated by using a larger array with higher N. 2) The Rx transducer directivity, meaning that a disc-shaped transducer cannot collect US pressure at large angles. Therefore, future research is needed to improve the directivity of the Rx transducer in US WPT links (similar to the hydrophone used in our measurements). Note that the beam widths in Figs. 17c and 17d at $\theta_s \neq 0$ are not the same as axial and lateral HPBW.

Fig. 17 also shows the measured P_L of the link in the presence of the chicken breast when the beam was focused at F = 20 with θ_s of 0° and 30°. The effect of tissue on P_L was minimal as P_L reduced slightly from 6.1 mW to 6 mW at θ_s of 0° and from 2 mW to 1.8 mW at θ_s of 30°.

Although the P_L values in Fig. 17 are lower at $\theta_s \geq$ 30° even with beam focusing and steering, Fig. 18 shows that P_L could be much smaller without beam steering. The P_L values in Fig. 18 were measured in three scenarios. 1) The beam was focused at F = 20 mm and θ_s = 0°, and Rx was moved along the axial axis $\boldsymbol{x}$ ($\boldsymbol{y}$ = $\boldsymbol{z}$ = 0), resulting in the peak P_L of 6.1

mW. 2) The beam was focused at F = 20 mm and θ_s = 45°, and Rx was moved in parallel with the ***x*** axis around the focal spot (***y*** = 13.2 mm, ***z*** = 0), resulting in the peak P_L of 0.8 mW. 3) The beam was focused at F = 20 mm and θ_s = 0°, but Rx was moved in parallel with ***x*** axis at ***y*** = 13.2 mm (***z*** = 0; i.e., condition of implant movement without refocusing), resulting in the peak P_L of 0.02 mW. Therefore, steering the beam at 45° resulted in 40-fold higher P_L, which is quite significant. Improving the Rx transducer directivity can further improve these results.

Table II compares the key parameters of our link against recent US WPT links for powering mm-sized biomedical implants. In our previous work [25], a single disc-shaped transducer has been used as Tx and a PTE of 0.65% has been achieved at 30 mm distance. However, this link does not have the capability of beam steering and focusing, suffering from a poor PTE of ~ 0.02% (~ 32-fold drop) with only 6 mm misalignment (in ***y*** direction in Fig. 3). By contrast, our fabricated link in this work achieves a much higher PTE of ~0.13% in the same condition (only 10% drop based on Fig. 17d). This shows the significance of beam steering and focusing with an array in addition to providing the capability of powering multiple implants.

In [28] and [32], ring and circular transducers in circular-and hexagonal-shaped Tx arrays have been used, respectively. The high PTE of 4% in [32] at a large F of 50 mm is due to its large Rx size (D_{Rx} = 11 mm). In [30], a linear 32-element array has been demonstrated and characterized with no Rx transducer. The calculated PTE of 1% is based on the acoustic pressure, neglecting Rx efficiency and R_L. The 52-element 2D array in [31] achieves a PTE of 0.018% at a 5 cm depth, and the PTE has dropped by ~ 10-fold at the steering angles of ±30° (at 2 cm depth). The small array in [33] operates at a high f_c of 8.4 MHz with high attenuation in tissue to deliver power at small F of 5 mm. This paper presents the attempt towards co-optimizing the geometries of both Tx beamforming array and Rx transducers as well as fc considering design constraints from the application and fabrication.

V. Discussion

In this paper, which mainly focuses on the design and optimization of US WPT links with a phased array, the US transducers in the array and Rx did not include any acoustic matching layer for simplicity. It is well known that for optimal US transfer between two media (e.g., piezoelectric material, tissue) with different acoustic impedances (Z), acoustic matching can help to reduce the US reflections at the boundary [46]. For the fabricated US WPT link, the acoustic impedances of PZT-5A and tissue are Z_1 = 31.5 MRayls and Z_2 = 1.6 MRayls, respectively. Therefore, for optimal acoustic matching, the thickness and acoustic impedance of the matching layer should be $\lambda/4$ and $(Z_1 \times Z_2)^{0.5}$, respectively [47]. We have already discussed the effect of matching layer in our previous works in [25] and [44]. For example, similar to [44], Alumina can be added as the matching layer.

It is well established that compared to RF/inductive links, US WPT links can deliver more power with higher PTE to deeply implanted mm-sized devices [25]. Table III compares the performance of our fabricated US link with phase array to state-of-the-art RF and inductive links. The low PTE and P_L in [7] and [26] with powering distance of ~ 50 mm indicates

that RF/inductive links are not optimal for powering deeply implanted devices. Note that the Rx size is 9.4 mm^3 in [7], which is ~ 10-fold larger than our fabricated US Rx (1 mm^3). Based on Fig. 17a, increasing the distance to ~ 50 mm in the fabricated US WPT link (optimized for 20 mm) can still provide P_L of 1 mW with ~ 0.03% PTE. Optimizing the array for a larger distance, which will lead to larger aperture and N, will result in even much higher PTE and P_L. The works in [8] and [48] have achieved high P_L and PTE at a relatively short distance (12 mm in [8]). The 3-coil link in [48] requires the Rx coil to be located within the secondary coil, which reduces the distance effectively to zero. As it is well known, increasing the distance drastically reduces the mutual coupling between coils, thereby reducing PTE and P_L close to levels in [26].

There is still room for further improvement of the fabricated array PTE in this work. First, the fabricated array with limited $N = 16$ (due to the limitation of our current electronics) has a small aperture. Increasing its aperture size (and N) can improve PTE, particularly at larger depth. For instance, the optimal array in Table I with $N = 48$ achieves ~ 2.5-fold higher simulated FoM than that of the fabricated array with limited $N = 16$ at 20 mm powering distance. This implies that the optimal array PTE could potentially be ~ 2.5-fold higher. Second, the fabrication process can be improved by accessing more advanced fabrication tools. For instance, as shown in Figs. 9 and 10, there is some element-to-element variations in impedance and US pressure output. This could mainly be due to the mismatch of the material thickness of the backing and front layers. These variations not only reduce the electrical-mechanical conversion efficiency of each element, but also degrade the performance of the array in proper beamforming.

To accurately measure the beam profile of the array in the presence of electrical interference, only 6 pulses with a 1 ms interval delay were used to drive the array, while US WPT requires continuous driving of the array. Therefore, due to the limited input power, no thermal effect was observed in our measurements. In our future work, however, we will measure and study the generated heat in the array and its surrounding tissue when the array is driven by a continuous signal with the largest amplitude.

Depending on the power requirement, implant's size, and implantation depth, US WPT links with different sizes can be used in a wide variety of medical applications. In general, miniaturized implants for sensing and actuation applications (e.g., recording, stimulation, pressure sensing) in both the central and peripheral nervous systems (e.g., spinal cord, heart, stomach, bladder, to name a few) can benefit from US WPT links for mW-level power delivery at short distances (several mm) and sub-mW-level power delivery at large distances (several cm). Our target application for US WPT links is gastric-wave mapping through distributed small implants located inside the submucosal space [16]. Depending on the subject (human or animal), the implant depth can vary from several mm to several cm. In this paper a limited depth of tens of mm was achieved in measurements mainly due to the limitations of the commercial electronics (only 16 channels) for driving the US array. This significantly reduced the array aperture size (and N) and consequently reduced the powering depth. We are currently developing custom high-voltage drivers with much higher number of channels to further extend the range in our future work.

VI. Conclusion

A design methodology has been proposed to maximize the PTE of US links with a Tx array for WPT to mm-sized biomedical implants. The proposed design procedure helps designers identify the optimal geometries of Tx array (elements' width, length, thickness, spacing; array's aperture; its number of elements) and Rx transducer (diameter, thickness) as well as the optimal operation frequency (f_c) in an iterative process. An optimal FoM, which considers the link PTE, has been proposed to enable optimization of the Tx array in k-Wave, while the Rx transducer has been optimized in COMSOL. Our design procedure and k-Wave/COMSOL models have also been validated through measurements by optimizing a 16-element linear array for the Tx to power a 1 mm^3 Rx. The operation of the 1.1 MHz link with beam steering and focusing at F = 10–30 mm and θ_s = 0–60° has been demonstrated in measurements inside a water tank without and with tissue. This work presents a US WPT link, in which the geometries of both Tx array and Rx transducer as well as fc have been co-optimized with realistic design settings, for mm-sized biomedical implants.

Acknowledgments

This work was supported by the National Institutes of Health (NIH) under Grant R21EY030700.

References

[1]. Chen K, Yang Z, Hoang L, Weiland J, Humayun M, and Liu W, "An integrated 256-channel epiretinal prosthesis," IEEE J. Solid State Cir, vol. 45, pp. 1946–1956, Sep. 2010.

[2]. McConnell G, Rees H, Levey A, Gutekunst C, Gross R, and Bellamkonda R, "Implanted neural electrodes cause chronic, local inflammation that is correlated with local neurodegeneration," J. Neural Eng, vol. 6, p. 056003, Oct. 2009. [PubMed: 19700815]

[3]. Sekhon B, "Bioelectronic medicine/electroceuticals – The emergence of new electronic therapeutics," Int. J. Nov. Res. Eng. Pharm. Sci, vol 1, pp. 58–63, Mar. 2014.

[4]. Kiani M, Jow UM, and Ghovanloo M, "Design and optimization of a 3-coil inductive link for efficient wireless power transmission," IEEE Trans. Biomed. Cir. Syst, vol. 5, no. 6, pp. 579–591, Dec. 2011.

[5]. Jow U and Ghovanloo M, "Design and optimization of printed spiral coils for efficient transcutaneous inductive power transmission," IEEE Trans. Biomed. Cir. Syst, vol. 1, pp. 193–202, Sept. 2007.

[6]. Baker M and Sarpeshkar R, "Feedback analysis and design of RF power links for low-power bionic systems," IEEE Trans. Biomed. Cir. Syst, vol. 1, no. 1, pp. 28–38, Mar. 2007.

[7]. Ho J, Yeh A, Neofytou E, Kim S, Tanabe Y, Patlolla B, Beygui R, and Poon A, "Wireless power transfer to deep-tissue microimplants," Proc. Nat. Acad. Sci, vol. 111, pp. 7974–7979, Jun. 2014. [PubMed: 24843161]

[8]. Ahn D and Ghovanloo M, "Optimal design of wireless power transmission links for millimeter-sized biomedical implants", IEEE Trans. Biomed. Cir. Syst, vol. 10, no. 1, pp. 125–137, Feb. 2016.

[9]. Muller R, Le H, Li W, Ledochowitsch P, Gambini S, Bjorninen T, Koralek A, Carmena J, Maharbiz M, Alon E, and Rabaey J, "A minimally invasive 64-channel wireless μECoG implant," IEEE J. Solid-State Cir, vol. 50, pp.344–359, Jan. 2015.

[10]. Ibrahim A and Kiani M, "A figure-of-merit for design and optimization of inductive power transmission links for millimeter-sized biomedical implants," IEEE Trans. Biomed. Cir. Syst, vol. 10, no. 6, pp. 1100–1111, Dec. 2016.

[11]. Lin J, "A new IEEE standard for safety levels with respect to human exposure to radio-frequency radiation," IEEE Antennas Propag. Mag, vol. 48, pp. 157–159, 2006.

[12]. Edelman S, “Understanding ultrasound physics,” E.S.P Ultrasound 4 edition, July, 2012.

[13]. Food and Drug Administration (FDA), “Information for manufacturers seeking marketing clearance of diagnostic ultrasound systems and transducers” Guidance for Industry and FDA Staff, Sept. 9, 2008.

[14]. Seo D, Carmena J, Rabaey J, Alon E, and Maharbiz M, “Neural dust: an ultrasonic, low power solution for chronic brain-machine interfaces,” arXiv preprint arXiv: 1307.2196, 2013.

[15]. Seo D, Neely R, Shen K, Singhal U, Alon E, Rabaey J, Carmena J, and Maharbiz M, “Wireless recording in the peripheral nervous system with ultrasonic neural dust,” Neuron, vol. 91, pp. 529–539, Aug. 2016. [PubMed: 27497221]

[16]. Meng M and Kiani M, “Gastric seed: towards distributed ultrasonically interrogated millimeter-sized implants for large-scale gastric electrical-wave recording,” IEEE Trans. Cir. Syst. II, vol. 66, no. 5, pp. 1549–7747, May 2019.

[17]. Meng M, Graybill P, Ramos R, Javan-Khoshkholgh A, Farajidavar A, and Kiani M, “An ultrasonically powered wireless system for in vivo gastric slow-wave recording,” 41st IEEE Eng. Med. Biol. Conf., pp. 7064–7067, 2019.

[18]. Weber M, Yoshihara Y, Sawaby A, Charthad J, Chang T, and Arbabian A, “A miniaturized single-transducer implantable pressure sensor with time-multiplexed ultrasonic data and power links,” IEEE J. Solid-State Cir, vol. 53, no. 4, pp. 1089–1101, Apr. 2018.

[19]. Piech D, Johnson B, Shen K, Ghanbari M, Li K, Neely R, Kay J, Carmena J, Maharbiz M, and Muller R, “A wireless millimeter-scale implantable neural stimulator with ultrasonically powered bidirectional communication,” Nature Biomed. Eng, vol. 4, no. 2, pp. 207–222, 2020. [PubMed: 32076132]

[20]. Charthad J, Chang T.Ch., Liu Z, Sawaby A, Weber MJ, Baker S, Gore F, Felt SA, and Arbabian A, “A mm-sized wireless implantable device for electrical stimulation of peripheral nerves,” IEEE Trans. Biomed. Cir. Syst, vol. 12, no. 2, pp. 257–270, Apr. 2018.

[21]. Ghanbari MM, Piech DK, Shen K, Alamouti SF, Yalcin C, Johnson BC, Carmena JM, Maharbiz MM, Muller R, “A 0.8 mm^3 ultrasonic implantable wireless neural recording system with linear AM backscattering,” IEEE Int. Solid-State Cir. Conf, pp. 284–286, Feb. 2019.

[22]. Laursen K, Rashidi A, Hosseini S, Mondal T, Corbett B, and Moradi F, “Ultrasonically powered compact implantable dust for optogenetics,” IEEE Trans. Biomed. Circ. Syst, vol. 14, no. 3, pp. 583–594, Jun. 2020.

[23]. Shi C, Costa T, Elloian J, Zhang Y, and Shepard K, “A 0.065-mm^3 monolithically-integrated ultrasonic wireless sensing mote for real-time physiological temperature monitoring,” IEEE Trans. Biomed. Cir. Syst, vol. 14, no. 3, pp. 412–424, Jun. 2020.

[24]. Sonmezoglu S and Maharbiz MM, “A 4.5 mm^3 deep-tissue ultrasonic implantable luminescence oxygen sensor,” IEEE Int. Solid-State Cir. Conf, pp. 454–456, Feb. 2020.

[25]. Meng M and Kiani M, “Design and optimization of ultrasonic wireless power transmission links for millimeter-sized biomedical implants,” IEEE Trans. Biomed. Cir. Syst, vol. 11, no. 1, pp. 98–107, Feb. 2017.

[26]. Ibrahim A, Meng M, and Kiani M, “A comprehensive comparative study on inductive and ultrasonic wireless power transmission to biomedical implants,” IEEE Sens. J, vol. 18, no. 9, pp. 3813–3826, Mar. 2018. [PubMed: 30344453]

[27]. Ghanbari MM and Muller R, “Optimizing volumetric efficiency and backscatter communication in biosensing ultrasonic implants,” IEEE Trans. Biomed. Cir. Syst, vol. 14, no. 6, pp. 1381–1392, Dec. 2020.

[28]. Hosseini S, Laursen K, Rashidi A, Mondal T, Corbett B, and Moradi F, “S-mrut: Sectored-multi ring ultrasonic transducer for selective powering of brain implants,” IEEE Trans. Ultras. Ferr. Freq. Cont, vol. 68, pp. 191–200, Jan 2021.

[29]. Chang T, Weber M, Charthad J, Baltsavias S, and Arbabian A, “End-to-end design of efficient ultrasonic power links for scaling towards sub-millimeter implantable receivers,” IEEE Trans. Biomed. Cir. Syst, vol. 12, pp. 1100–1111, Oct. 2018.

[30]. Wang M, Chang T, Teisberg T, Weber M, Charthad J, and Arbabian A, “Closed-loop ultrasonic power and communication with multiple miniaturized active implantable medical devices,” IEEE Int. Ultrason. Symp, pp. 1–4, Sep. 2017.

[31]. Benedict BC, Ghanbari MM, Alamouti SF, Ersumo NT, and Muller R, “Time reversal beamforming for powering ultrasonic implants,” IEEE/EMBS Conf. Neural Eng., pp.647–650, May 2021.

[32]. Tseng V, Bedair S, and Lazarus N, “Phased array focusing for acoustic wireless power transfer,” IEEE Trans. Ultrason., Ferroelectr., Freq. Cont, vol. 65, no. 1, pp. 39–49, Jan. 2018.

[33]. Costa T, Shi C, Tien K, Elloian J, Cardoso F, and Shepard K, “An integrated 2D ultrasound phased array transmitter in CMOS with pixel pitch-matched beamforming,” IEEE Trans. Biomed. Cir. Syst, vol. 15, pp. 731–742, Aug. 2021.

[34]. Von Ramm O and Smith S, “Beam steering with linear arrays,” IEEE Trans. Biomed. Eng, vol. BME-30, pp. 438–452, Aug. 1983.

[35]. Wooh S and Shi Y, “Optimum beam steering of linear phased arrays,” Wave Motion, vol. 29, pp. 245–265, Apr. 1999.

[36]. Duerinckx A, “Matched gaussian apodization of pulsed acoustic phased arrays,” Ultrasonic Imaging, vol. 2, pp. 338–369, Oct. 1980. [PubMed: 7196618]

[37]. Treeby B and Cox B, “k-Wave: MATLAB toolbox for the simulation and reconstruction of photoacoustic wave fields,” J. Biomed. Opt, Apr. 2010.

[38]. Martin E, Jaros J, and Treeby B, “Experimental validation of k-Wave: nonlinear wave propagation in layered, absorbing fluid media,” IEEE Trans. Ultras. Ferroelect. Freq. Contr, vol. 67, pp. 81–91, Jan. 2020.

[39]. Shankar H and Pagel P, “Potential adverse ultrasound-related biological effects: A critical review,” Anesthesiology, vol. 115, pp. 1109–1124, 2011. [PubMed: 21866043]

[40]. Poelma C, “Ultrasound imaging velocimetry: a review,” Experiments in Fluids, vol. 58, p. 3, Dec. 2016.

[41]. Meng M and Kiani M, “Self-image-guided ultrasonic wireless power transmission to millimeter-sized biomedical implants,” IEEE 41st Eng. Med. Biol. Conf., July 2019.

[42]. Kashani Z and Kiani M, “Optimal ultrasonic pulse transmission for miniaturized biomedical implants,” IEEE Biomed. Cir. Syst. Conf, Oct. 2019.

[43]. Lerch R, “Simulation of piezoelectric devices by two- and three-dimensional finite elements,” IEEE Trans. Ultrason., Ferroelect., Freq. Contr, vol. 37, pp. 233–247, 1990.

[44]. Sadeghi Gougheri H, Dangi A, Kothapalli S, and Kiani M, “A comprehensive study of ultrasound transducer characteristics in microscopic ultrasound neuromodulation,” IEEE Trans. Biomed. Cir. Syst, vol. 13, pp. 835–847, Oct. 2019.

[45]. Uchino K, Zhuang Y, and Ural S, “Loss determination methodology for a piezoelectric ceramic: new phenomenological theory and experimental proposals,” J. Adv. Dielect, vol. 1, pp. 17–31, Jan. 2011.

[46]. Chen P, Wu P, Wan X, Wang Q, Xu C, Yang M, Feng J, Hu B, and Luo Z, “Ultrasound-induced wireless energy harvesting: from materials strategies to functional applications”, Nano Energy, vol. 77, 2020.

[47]. Zhou Q, Lam K, Zheng H, Qiu W, and Shung K, “Piezoelectric single crystals for ultrasonic transducers in biomedical applications,” Progress in Materials Science, vol. 66, Oct. 2014.

[48]. Mirbozorgi S, Yeon P, and Ghovanloo M, “Robust wireless power transmission to mm-sized free-floating distributed implants,” IEEE Trans. Biomed. Cir. Syst, vol. 11, pp. 692–702, Jun. 2017.

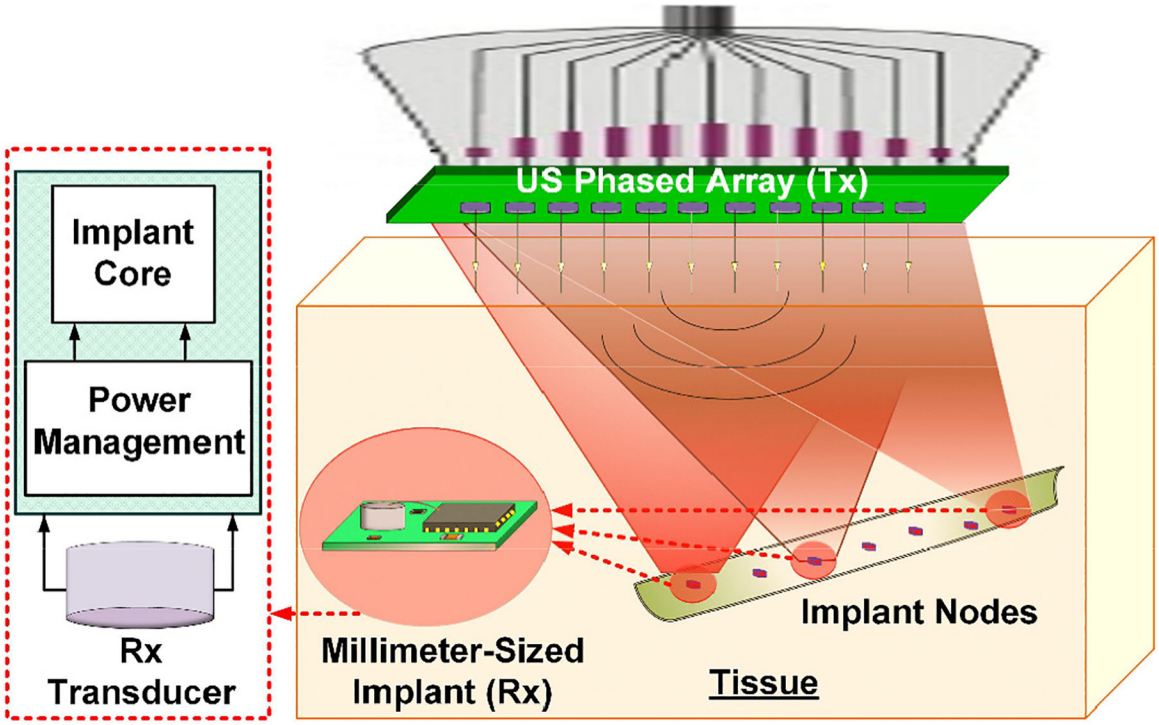

Fig. 1.

Conceptual schematic of a US WPT link for powering mm-sized implants uisng a US phased array as the power transmitter (Tx).

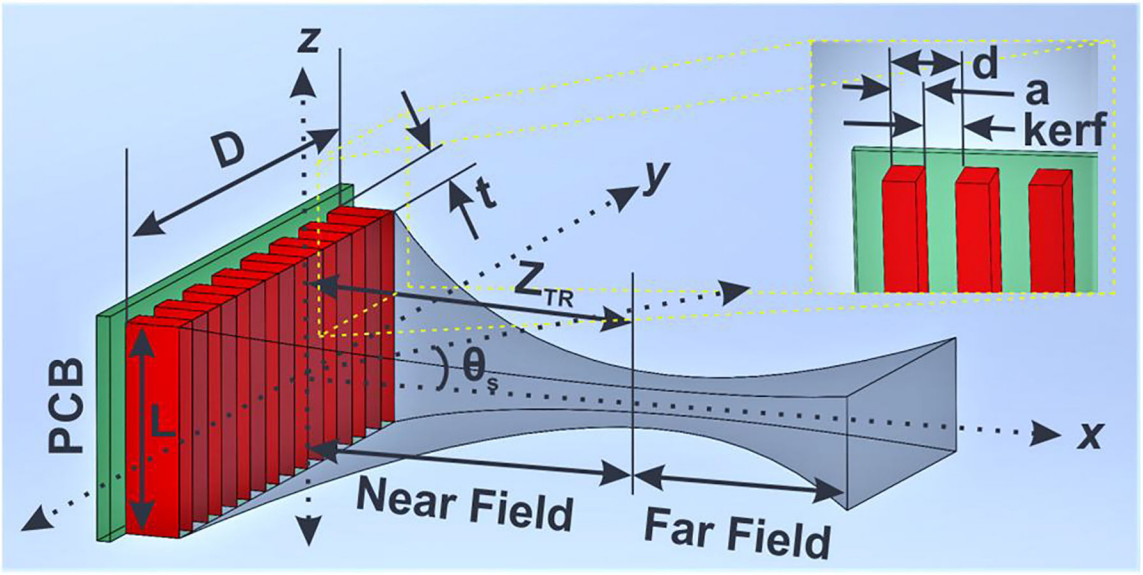

Fig. 2.

A linear US phased array with a conceptual beam shape, consisting of near- and far-field zones.

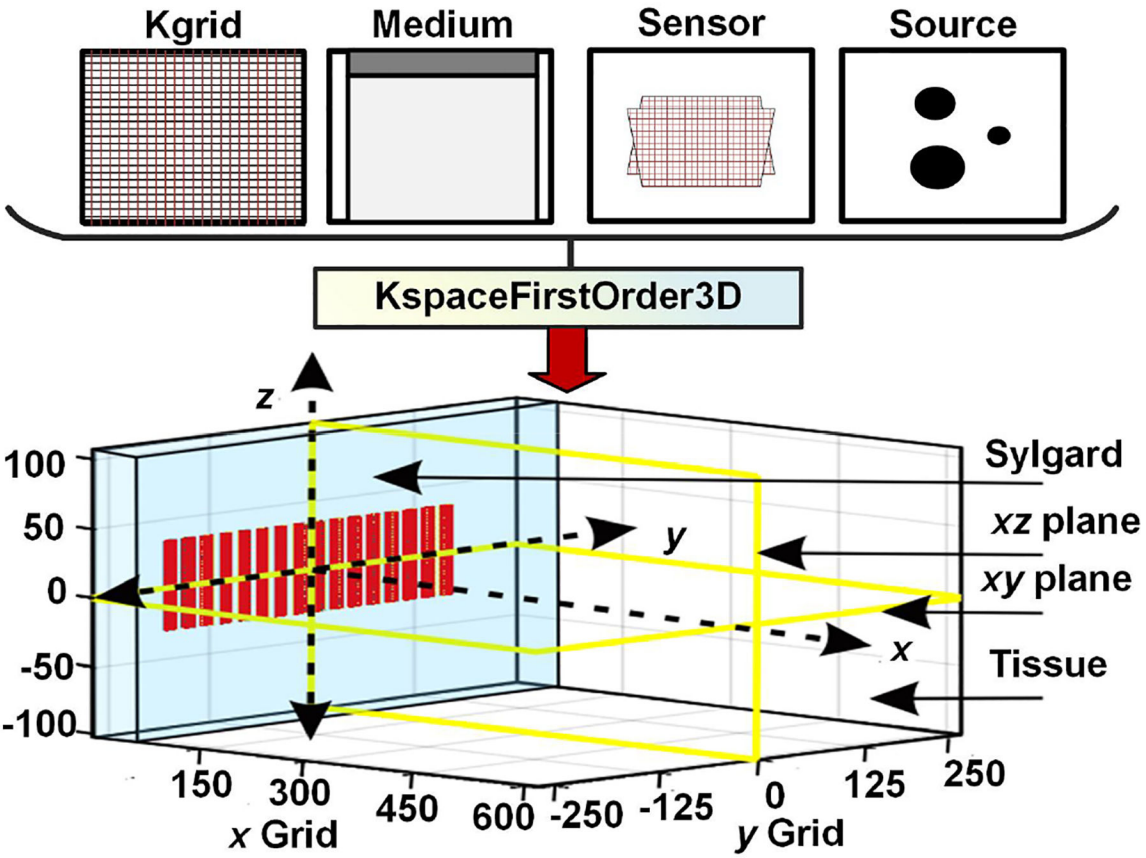

Fig. 3.

k-Wave simulation setup used to optimize an array for US WPT. The array surface is parallel to the ***yz*** plane and centered at the origin ***x*** = ***y*** = ***z*** = 0. Both the ***xy*** and ***xz*** planes were defined as sensors for recording US pressure.

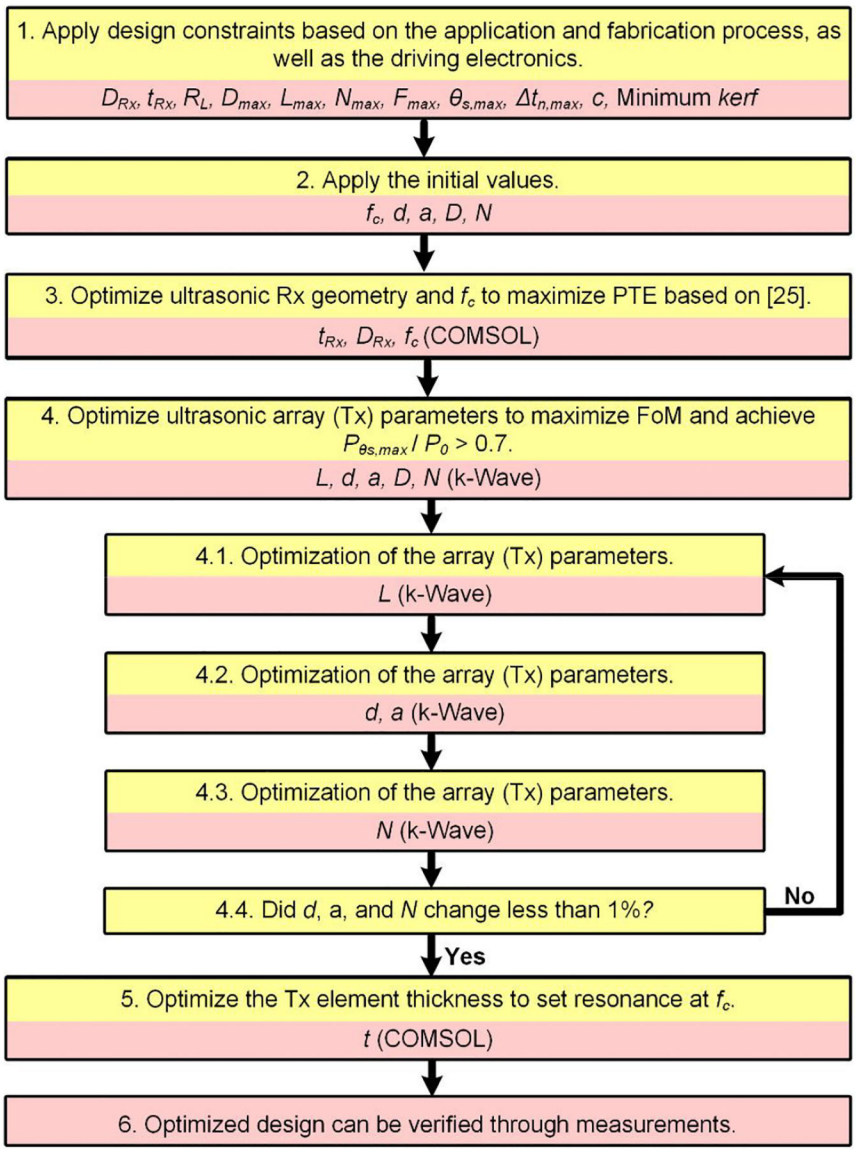

Fig. 4.

Iterative optimization flowchart of a US link with a phased array for efficient WPT to mm-sized biomedical implants. The proposed procedure needs to be completed in COMSOL and k-Wave.

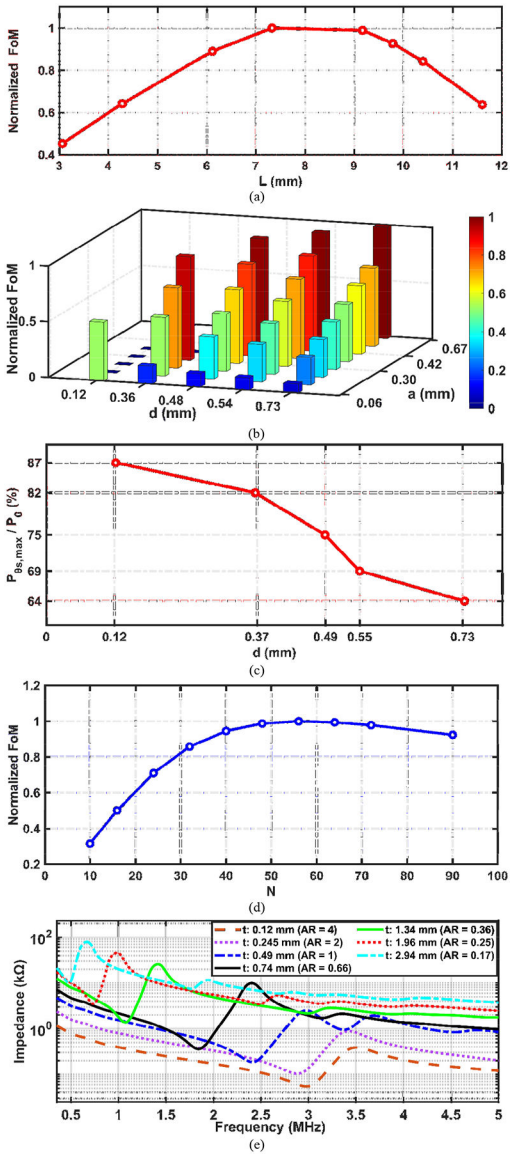

Fig. 5.

Geometry optimization of the US array at f_c =1.4 MHz, F = 30 mm, and $P_{\theta_{s,\,max}}/P_0 \geq 0.7$ at $\theta_{s,max}$ = 45°, showing (a) normalized FoM vs. L, (b) normalized FoM vs. d and a, (c) $P_{\theta_{s,\,max}}/P_0$ at $\theta_{s,max}$ = 45° vs. d, (d) normalized FoM vs. N, and (e) array element impedance vs. frequency to find optimal t.

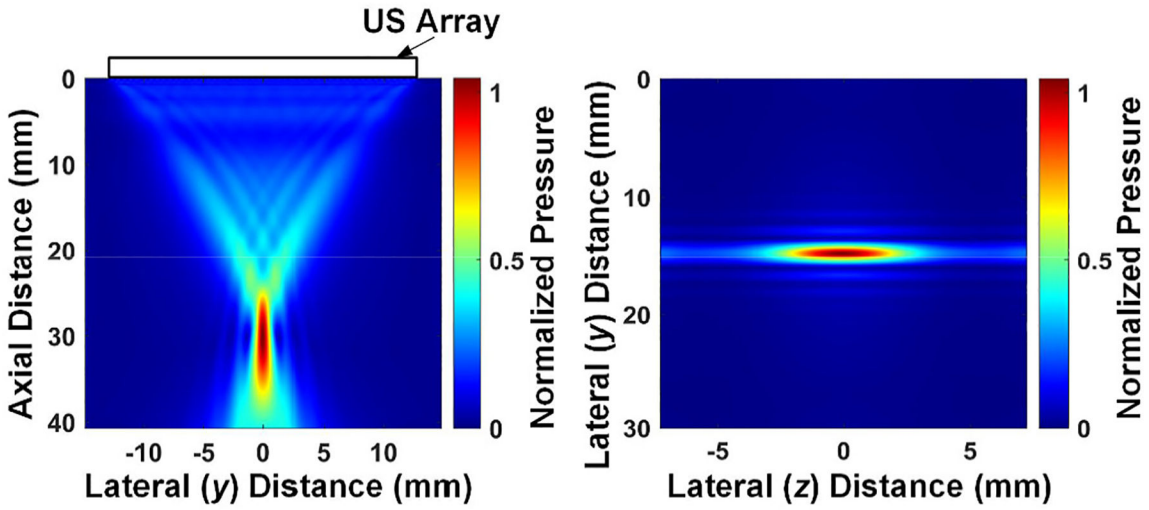

Fig. 6.

Simulated beam profiles of the optimal array in the ***xy*** and ***yz*** planes when the beam was focused at $F = 30$ mm and $\theta_s = 0°$ ($f_c = 1.4$ MHz).

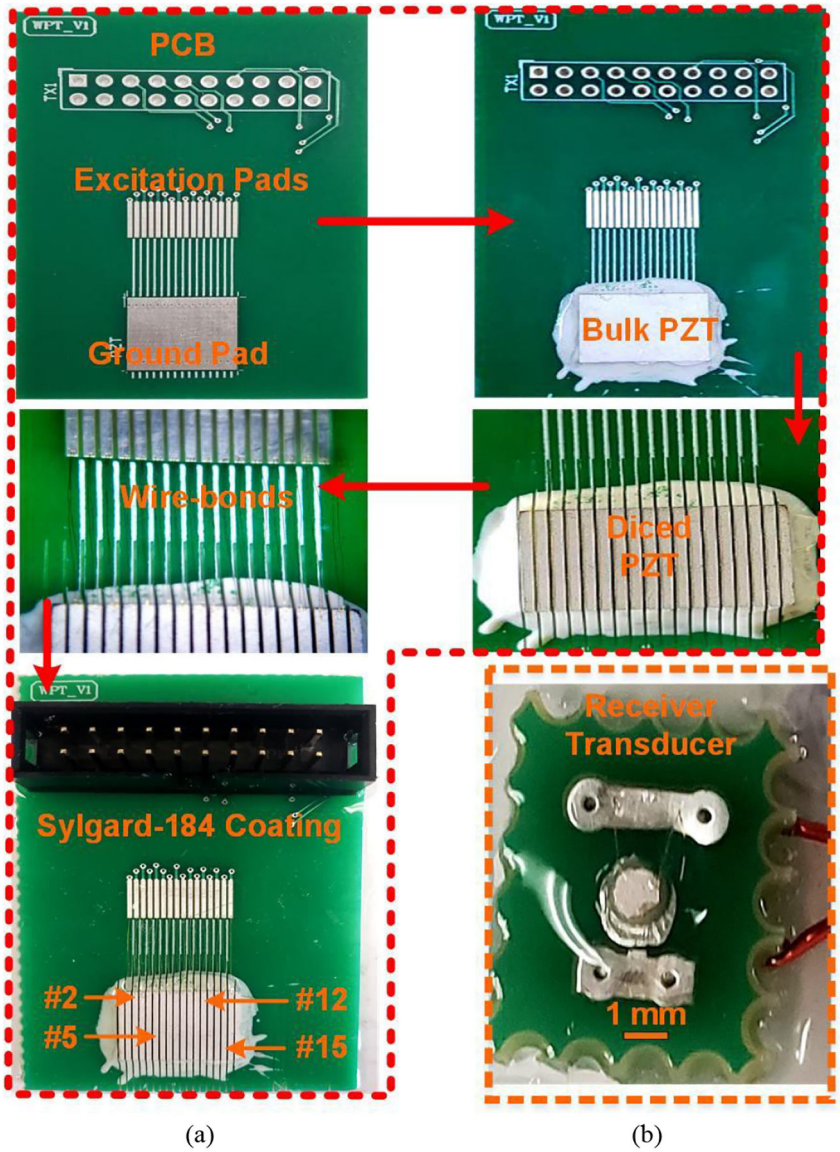

Fig. 7.

(a) Fabrication procedure of the linear US array using a dicing machine. (b) Fabricated mm-sized US receiver (Rx).

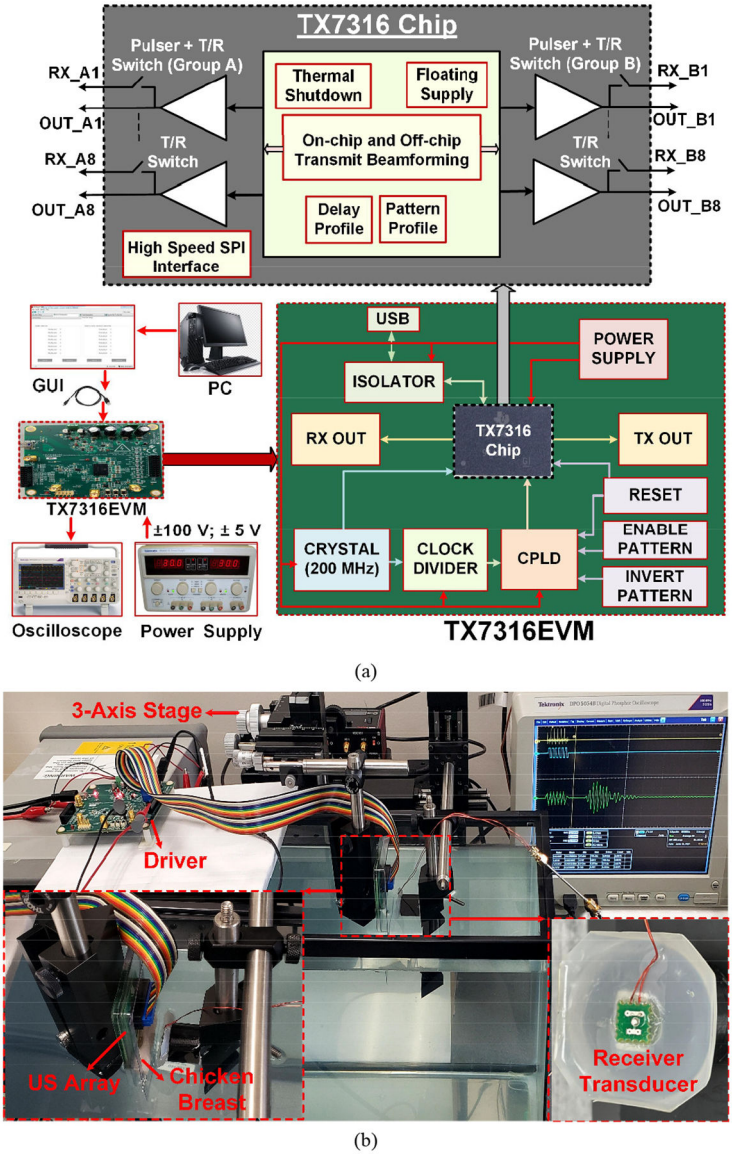

Fig. 8.

(a) Block diagram of the TX7316EVM evaluation board for driving the US array in our measurements. (b) Ultrasonic WPT link measurement setup inside a water tank without and with a chicken breast mimicking tissue.

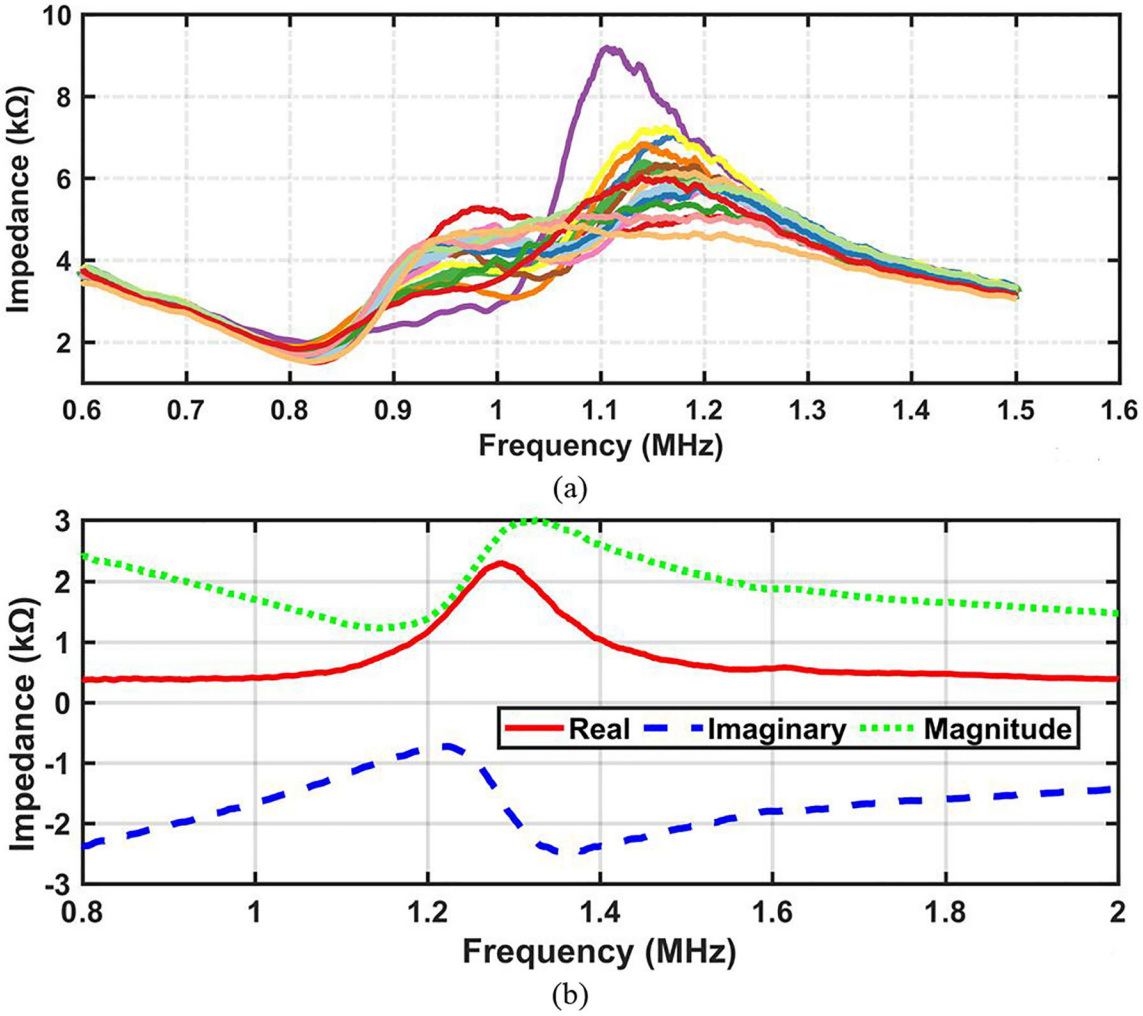

Fig. 9.

Measured impedance profile of (a) all 16 elements of the fabricated linear US array at a frequency range of 0.6–1.5 MHz, and (b) Rx transducer at a frequency range of 0.8–2 MHz.

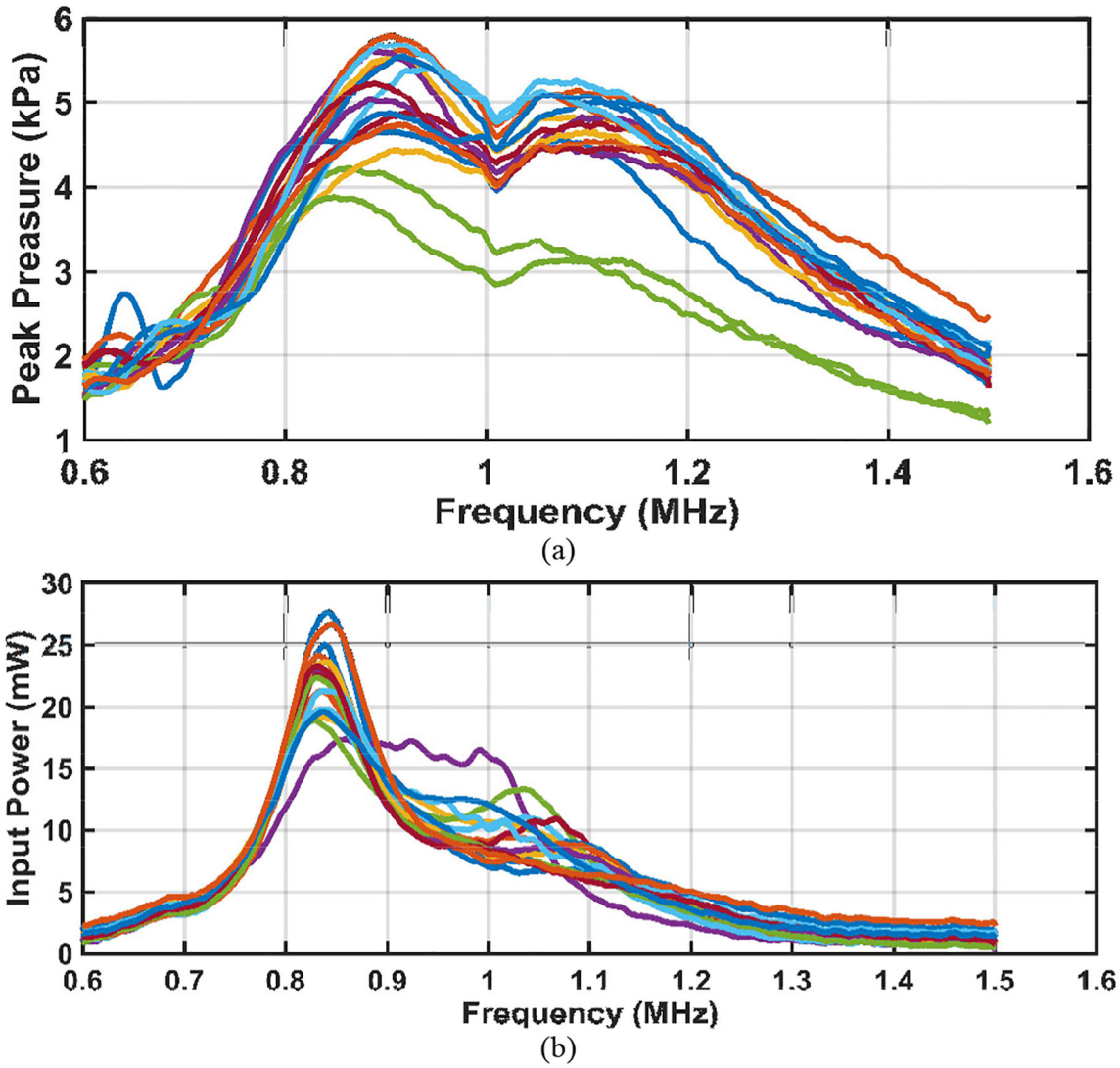

Fig. 10.

(a) Measured US pressure output at 20 mm axial distance (20 V peak-peak sinusoids) of individual elements in the fabricated 16-element array, and (b) measured electrical input power of each element at the same conditions.

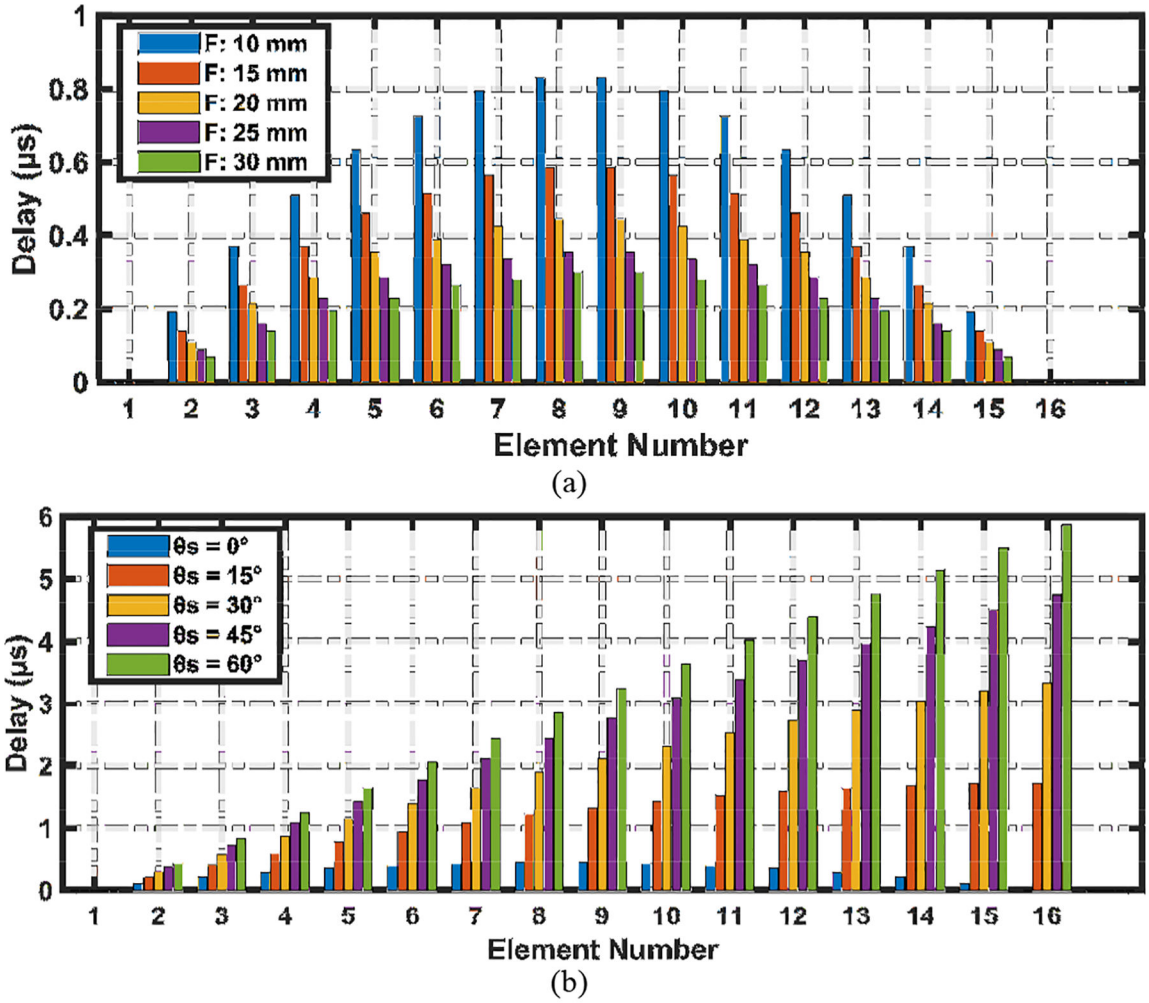

Fig. 11.

Optimal delay patterns of each element of US array obtained from k-Wave simulations for beamforming (a) at different focal depths F with $\theta_s = 0°$, and (b) at different steering angles θ_s with $F = 20$ mm.

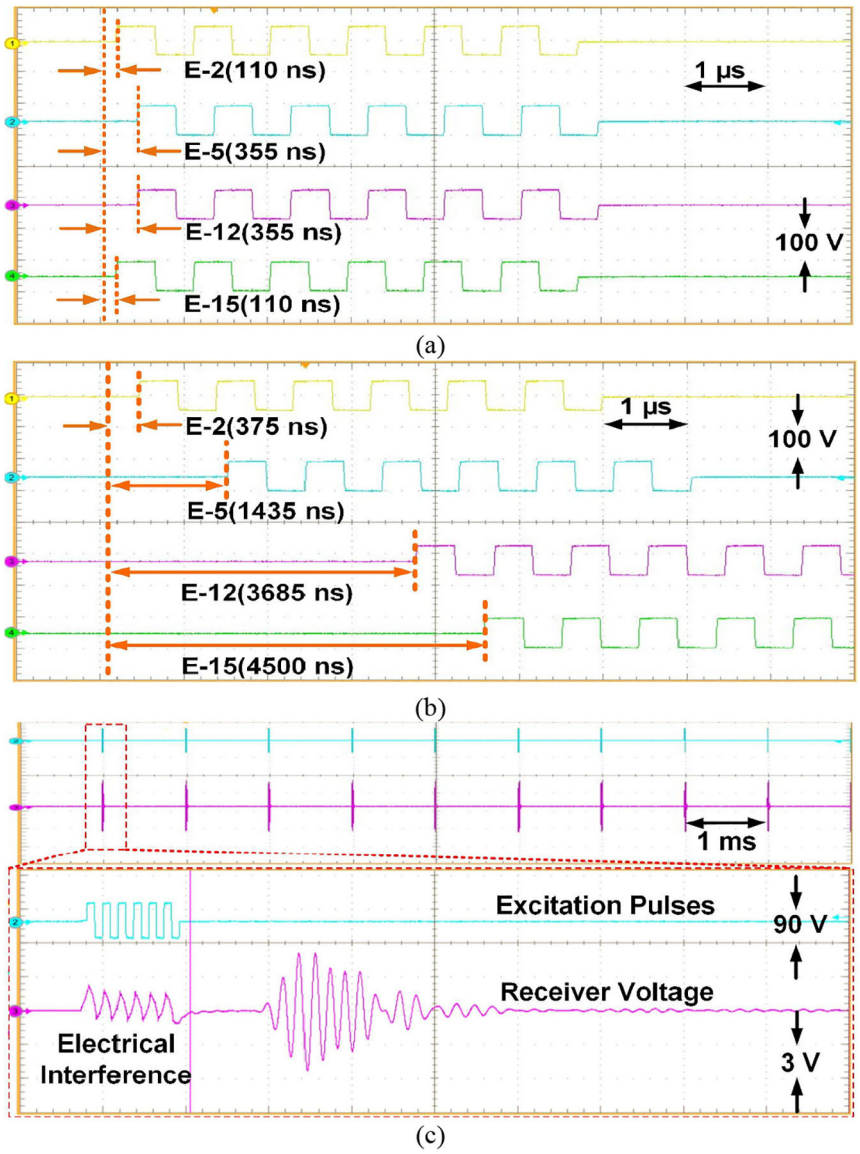

Fig. 12.

Measured transient waveforms of the driver board across 4 US elements (# 2, 5, 12, 15 in Fig. 7) for beamforming at $F = 20$ mm with (a) $\theta_s = 0°$ and (b) $\theta_s = 45°$. (c) Burst-mode signal generated by the driver and the received voltage by the Rx transducer ($F = 20$ mm, $\theta_s = 0°$).

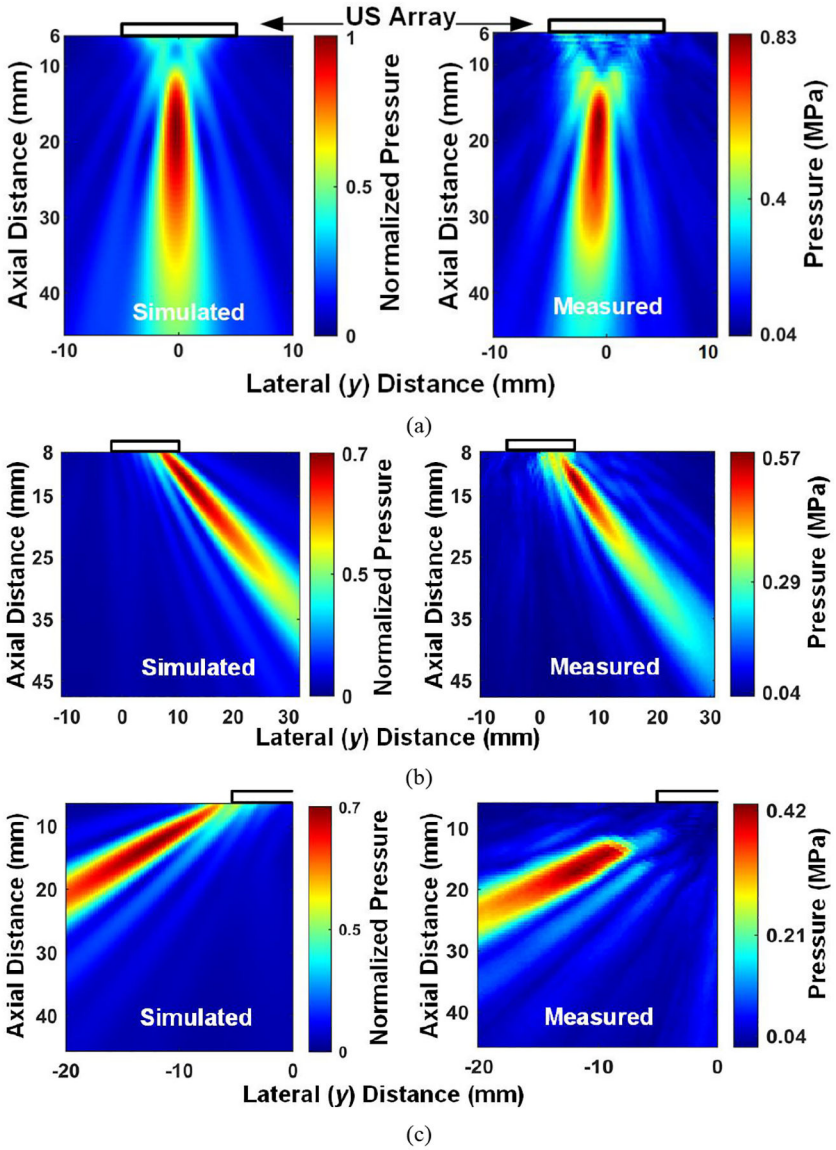

Fig. 13.

Simulated and measured beam profiles of the 16-element array in the ***xy*** plane at $F = 20$ mm with different θ_s of a) 0°, b) 45°, and c) −45°

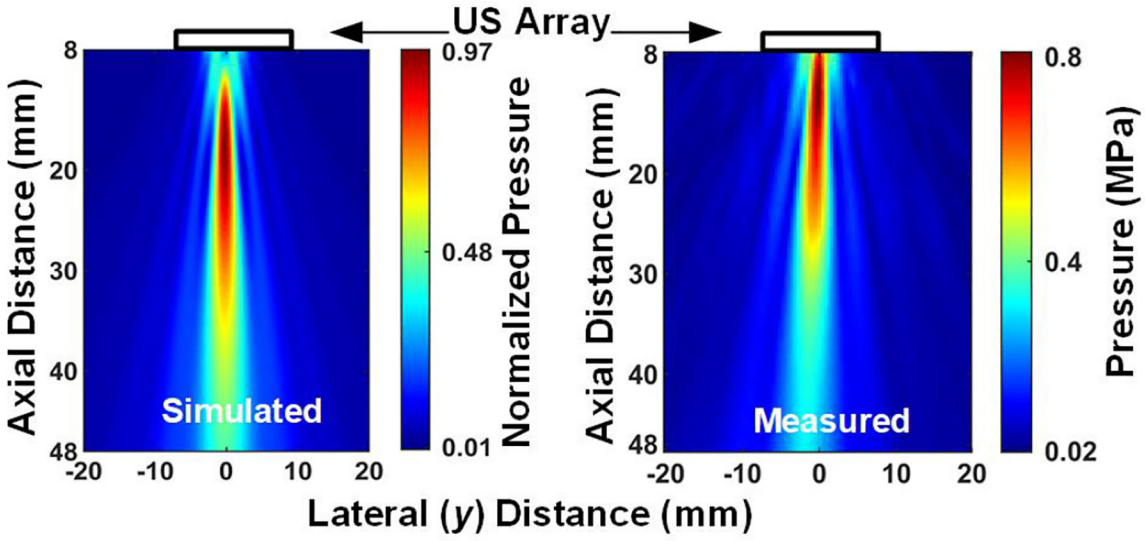

Fig. 14.

Simulated and measured beam profiles of the 16-element array in the ***xy*** plane at $F = 20$ mm ($\theta_s = 0°$) in the presence of the chicken breast.

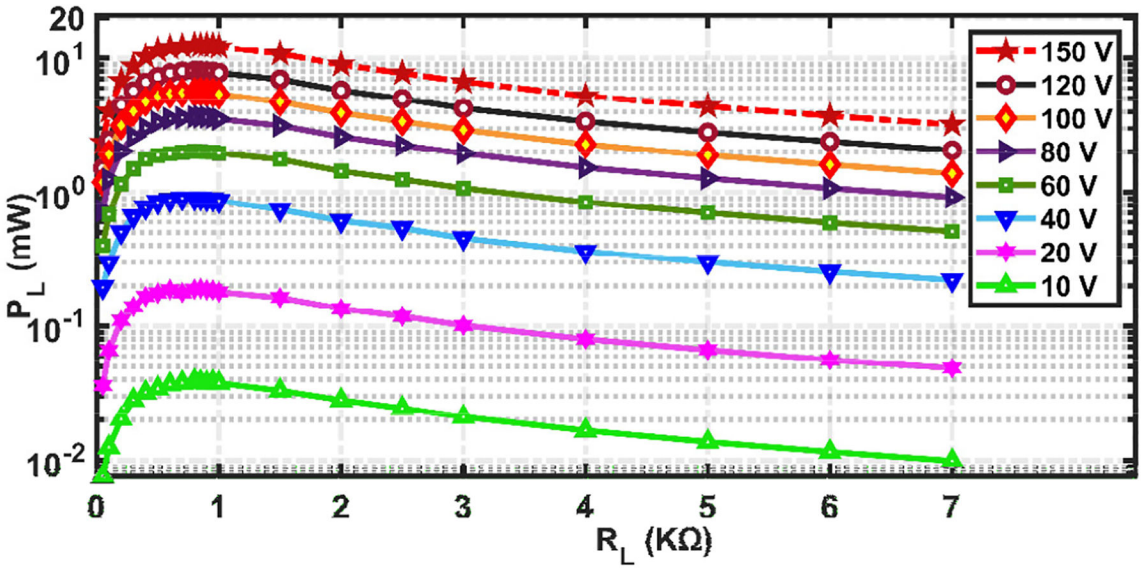

Fig. 15.

Measured received power P_L ($\theta_s = 0°$) by the Rx transducer vs. R_L at a depth of $F = 20$ mm while driving the array at different voltages.

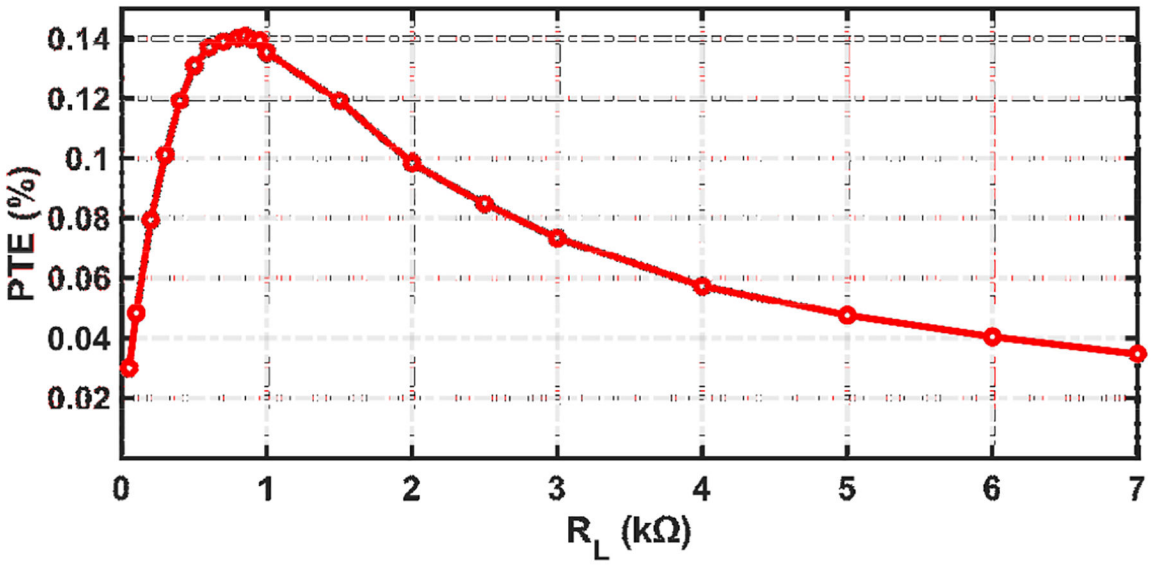

Fig. 16.

Measured highest PTE of the US WPT link for different *RL*, when the beam was focused at $F = 20$ mm ($\theta_s = 0°$).

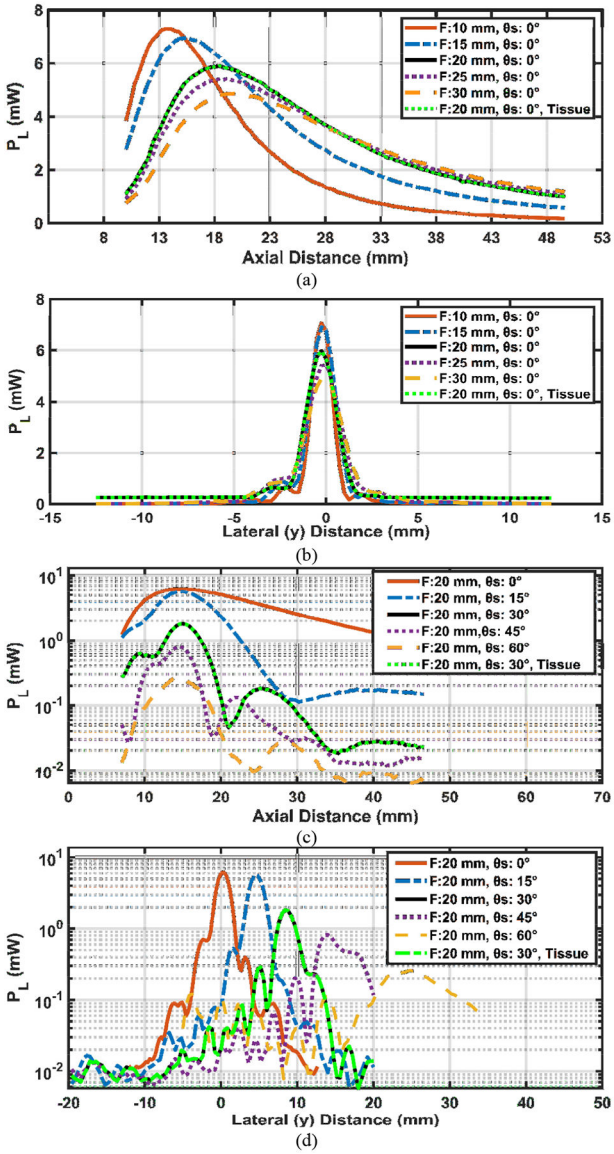

Fig. 17.

Measured P_L with beam focusing and steering at different F and θ_s (R_L = 850 Ω). (a) P_L at different axial distances at different F. (b) P_L at different lateral distances at different F. (c) P_L at different axial distances at different θ_s, and (d) P_L at different lateral distances at different θ_s.

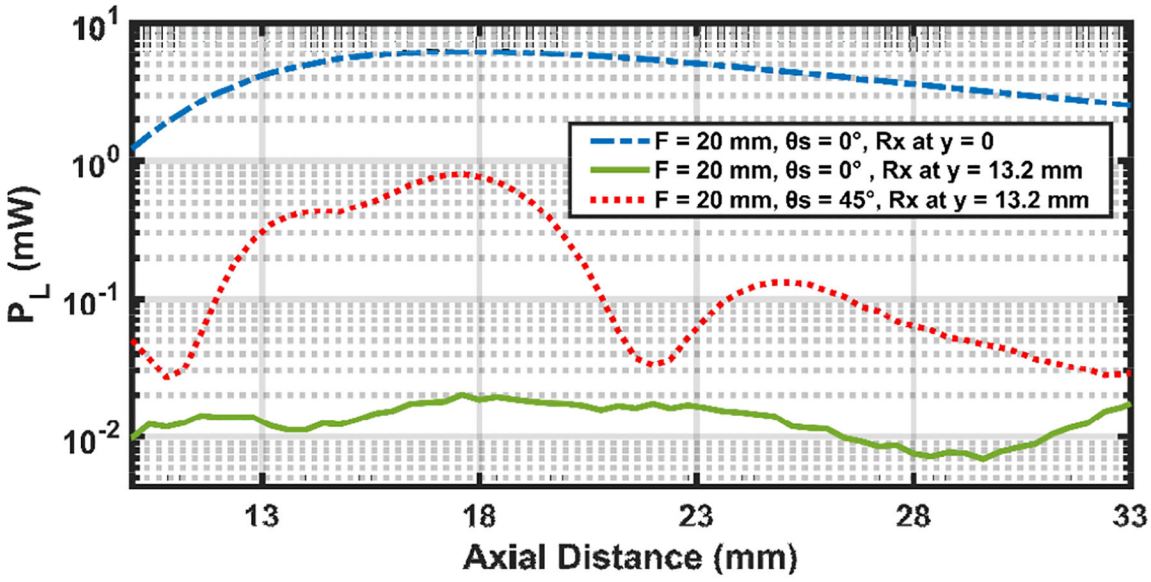

Fig. 18.

Measured *PL* along the axial axis ***x*** at zero and 13.2 mm lateral (***y***) distances when the beam was focused at $F = 20$ mm and $\theta_s = 0°$ and 45°.

Table I

Specifications of the Optimized US WPT Link for the Design Example and Measurements

Parameters	Symbols	Optimal-Design Link	Meas. Link
Tx Element Length (mm)	L	7.3	9
Tx Element Width (mm)	a	0.49	0.54
Tx Interelement Spacing (mm)	d	0.55	0.69
Tx Array Aperture (mm)	D	26	10.9
Tx Number of Elements	N	48	16
Tx Kerf (μm)	$kerf$	61	150
Tx Element Thickness (mm)	t	1.34	1.7
Rx Diameter (mm)	D_{RX}	1.2	1.1
Rx Thickness (mm)	t_{Rx}	0.7	1
Operation Frequency(MHz)	f_c	1.4	1.1
Powering Distance (mm)	F	30	20
Safety Factor	SF	1.5	
Load Resistance (kΩ)	R_l	2.5	0.85

Table II

Benchmarking of Recent Ultrasonic WPT Links for mm-Sized Biomedical Implants

	Parameters	Symbols	This work	[25]	[28]	[30]	[31]	[32]	[33]
Tx	Number of Elements	N	16 – 1D	1	8 – S-MRUT	32 – 1D	52 – 2D	37 – Hexagonal	676 – 2D
	Element Size (mm^2)	$a \times L$	0.54×9	-	-	0.5×1.6	0.8×0.8	8.4	0.05×0.05
	Element Thickness (mm)	t	1.7	1.95	0.5	1.44	0.8	-	0.26
	Aperture Size (mm)	D	10.9	15.9	3.8	23	13	70	4×5
Rx	Diameter (mm)	D_{Rx}	1.1	1.1	0.5	-	0.8	11	-
	Thickness (mm)	t_{Rx}	1	1	0.5	-	0.8	-	-
Ultrasonic Transducer Material		-	PZT-5A	PZT-4A	PZT-4	PZT-4	PZT-5A	Murata, Ma40s4s	PZT-5A
WPT Medium		-	Water/Tissue	Castor Oil	Water	Castor Oil	Oil	Air	Water
Operation Frequency (MHz)		fc	1.1	1.1	2.9	1.1	1.5	0.04	8.4
Powering Distance (mm)		F	18	30	1–3	50	50	50	5
Maximum Steering Angle (deg)		θ_s	±45	0	-	~ 20	±30	80	±15
Tx Peak-Peak Voltage (V)		-	100	-	-	16	±5	9	5
Delivered Power (mW)		P_L	6	-	-	-	0.013	15	-
*Power Transfer Efficiency (%)		PTE	0.14	0.65	-	1**	0.018***	4	-
Power Transfer Efficiency with 6 mm Misalignment (%)		PTE	0.13	0.02	-	-	-	-	-

* Reported at $\theta_S = 0°$.

** No Rx transducer (calculated for a 1 mm^2 Rx).

*** Each element consumes 1.4 mW while delivering P_L of 13 µW.

Table III

Comparison of Fabricated US WPT Link to Inductive/RF Links

Parameters	This work (US)	[7] 2-Coil	[8] 2-Coil	[26] 2-Coil	[48] 3-Coil
Rx Volume (mm^3)	~ 1	9.4	1	1.1	~ 0.5
Powering Dist. (mm)	18	50	12	52	**0
Operation Freq. (MHz)	1.1	1600	200	20	60
PTE (%)	0.14	0.04	0.56	0.0064	2.4
Power, P_L (mW)	*6	0.2	0.22	0.0056	1.3

* 100 V pulses across the array.

** L_2-L_4 spacing.